Fast Probabilistic Seismic Hazard Analysis through Adaptive Importance Sampling

Soung Eil Houng*[1] and Luis Ceferino[1]

ABSTRACT

Probabilistic Seismic Hazard Analysis (PSHA) traditionally relies on two computationally intensive approaches: (a) Riemann Sum and (b) conventional Monte Carlo (MC) integration. The former requires fine slices across magnitude, distance, and ground motion, and the latter demands extensive synthetic earthquake catalogs. Both approaches become notably resource-intensive for low-probability seismic hazards, where achieving a COV of 1% for a 10^{-4} annual hazard probability may require 10^8 MC samples. We introduce Adaptive Importance Sampling (AIS) PSHA, a novel framework to approximate optimal importance sampling (IS) distributions and dramatically reduce the number of MC samples to estimate hazards. We evaluate the efficiency and accuracy of our proposed framework using Pacific Earthquake Engineering Research Center (PEER) PSHA benchmarks that cover various seismic sources, including areal, vertical, and dipping faults, as well as combined types. Our approach computes seismic hazard up to 3.7×10^4 and 7.1×10^3 times faster than Riemann Sum and traditional MC methods, respectively, maintaining COVs below 1%. We also propose an enhanced approach with a "smart" AIS PSHA variant that leverages the sampling densities from similar ground motion intensities. This variant outperforms even "smart" implementations of Riemann Sum with enhanced grid discretizations by a factor of up to 130. Moreover, we demonstrate theoretically that optimal IS distributions are equivalent to hazard disaggregation distributions. Empirically, we show the approximated optimal IS and the disaggregation distributions are closely alike, e.g., with a Kolmogorov–Smirnov statistic between 0.017 and 0.113. This approach is broadly applicable, especially for PSHA cases requiring extensive logic trees and epistemic uncertainty.

1. Civil and Environmental Engineering, University of California, Berkeley, California, U.S.A, https://orcid.org/0000-0001-6873-5327 (SEH) https://orcid.org/0000-0003-0322-7510 (LC)

*Corresponding author: shoung@berkeley.edu

Cite this article as Houng, Soung Eil and Luis, Ceferino (2022). Fast Probabilistic Seismic Hazard Analysis through Adaptive Importance Sampling, *Bull. Seismol. Soc. Am.* **0**, 1–35, doi: 00.0000/0000000000.

KEY POINTS

- The Adaptive Importance Sampling (AIS) is introduced for fast PSHA computations.
- AIS PSHA is significantly faster than traditional numerical approaches and easily facilitates disaggregation.
- The approach is broadly applicable to PSHA involving extensive logic trees.

Supplemental Material

INTRODUCTION

Probabilistic Seismic Hazard Analysis (PSHA) has become a foundational method for determining seismic design levels and conducting regional seismic risk analyses since its first inception (Cornell, 1968; U. S. Nuclear Regulatory Commission, 2007; McGuire, 2008; ASCE, 2022; Kennedy et al., 1980; Ceferino et al., 2020; Silva et al., 2020; Baker et al., 2021; Papadopoulos and Bazzurro, 2021; Arora and Ceferino, 2023). Since we cannot solve PSHA analytically due to the complexity in seismic source and ground motion models, numerous researchers have developed computer software for PSHA computation (Cornell, 1968; McGuire, 1976; Kiremidjian et al., 1982; Field et al., 2003; Ordaz et al., 2013; Pagani et al., 2014). The existing software primarily employs Riemann Sum for numerical integration of PSHA (Thomas et al., 2010; Hale et al., 2018). The Riemann Sum offers robust PSHA integration with sufficiently dense grids. However, this method generally incurs a significant computational load exponentially increasing with the number of grids and dimensions in multi-dimensional integrations (Philippe and Robert, 2001). Furthermore, the results are highly sensitive to the chosen grid design, especially for low exceedance probabilities (Thomas et al., 2010; Hale et al., 2018). Alternatively, other software adopted Monte-Carlo (MC) integration for PSHA (Assatourians and Atkinson, 2013, 2019). MC integration calculates exceedance probabilities by generating random synthetic earthquake catalogs (Musson, 2000). MC's primary advantage lies in its straightforward concept compared to Riemann Sum (Musson, 2000; Dick et al., 2013). Nevertheless, MC framework requires a substantially-long synthetic catalog to accurately estimate hazards from rare events, especially for low exceedance probabilities, e.g., $p < 10^{-4}$ /yr (Kroese et al., 2014).

Importance Sampling (IS) can offer a solution to this rare event simulation (Tokdar and Kass, 2010). IS was initially introduced in statistical physics (Hammersley and Morton, 1954) to improve the computational efficiency of rare event simulation. IS relies on identifying an appropriate probability distribution ("IS distribution") to explore low-probability spaces effectively. Researchers use the IS distribution to sample rare events with a higher likelihood than conventional MC and then correct their frequency through weights, significantly reducing the number of samples to compute low probabilities (Robert et al., 1999). However, finding such an appropriate distribution can be challenging because the distribution differs for each problem being solved. Thus, many numerical experiments are often conducted first through trial-and-error to identify IS distributions, which is still computationally expensive.

In regional seismic risk analysis, numerous studies have been conducted to sample hazard-consistent earthquake ground motions (Crowley and Bommer, 2006; Kiremidjian et al., 2007; Jayaram and Baker, 2010; Han and Davidson, 2012; Manzour et al., 2016; Christou et al., 2018; Kavvada et al., 2022). Kiremidjian et al. (2007) first introduced IS distributions that sample large-magnitude earthquakes with a high probability to reduce the computational burden of seismic hazard and risk analyses. Jayaram and Baker (2010) expanded the approach by defining IS distributions to sample high-intensity ground motions. However, Jayaram and Baker (2010) highlighted the computational challenges to identify an effective IS distribution and ended up using K-mean clustering to reduce the number of ground motion samples. Rahimi and Mahsuli (2019) applied the IS sampling density as the normal distribution centered at the "design point" derived from the first- and second-order reliability method to PSHA computation.

To find effective IS distributions, computational statisticians have developed a general framework to find them through iterative algorithms denominated "Adaptive Importance Sampling (AIS)" (Bugallo et al., 2017). Various AIS algorithms have been introduced, e.g., cross-entropy based AIS, Vegas, Divonne, and Miser (Lepage, 1978; Friedman and Wright, 1981; Rubinstein, 1997; Press and Farrar, 1990; Rubinstein and Kroese, 2004; Bugallo et al., 2017). The application of AIS is widely adopted to solve the integration with high dimensions, such as in the field of statistical physics, finance, reliability engineering, and signal processing (Au and Beck, 2001; Kappen and Ruiz, 2016; Nieto and Ruiz, 2016; Bugallo et al., 2017). Although previous studies suggest the use of IS for PSHA calculation (Jayaram and Baker, 2010; Rahimi and Mahsuli, 2019), no research has been published regarding the use of AIS for this purpose. AIS can provide a general methodology for identifying an appropriate IS distribution for seismic hazards, eliminating computationally expensive experiments in the regular IS approach, whose efficiency typically depends on the researcher's experience in the field.

Among various AIS algorithms (Lepage, 1978; Friedman and Wright, 1981; Rubinstein, 1997; Press and Farrar, 1990; Rubinstein and Kroese, 2004; Bugallo et al., 2017), in this study, we apply the VEGAS algorithm for PSHA to leverage its straightforward mathematical framework and fast convergence. Thus, this study introduces a novel computational method for PSHA curve calculation using the AIS VEGAS algorithm (Lepage, 1978, 2021). This paper also shows that AIS facilitates hazard disaggregation, the relative contribution of each random variable to the overall hazard (Bazzurro and Cornell, 1999).

We explore three key aspects of the method: 1) the enhancement of computational efficiency and accuracy that the AIS algorithm offers over traditional methods; 2) the process of obtaining hazard disaggregation through AIS; and 3) the presentation of "smart" AIS to further improve the performance of the algorithm. We present the theoretical background of AIS PSHA and validate the method through numerical examples.

MATHEMATICAL FORMULATION

Probabilistic Seismic Hazard Analysis (PSHA)

At a site of interest, the annual rate of ground motion exceedance from a single source can be calculated as:

$$\lambda(X > a) = \nu \int_{\varepsilon_{\min}}^{\varepsilon_{\max}} \int_{r_{\min}}^{r_{\max}} \int_{m_{\min}}^{m_{\max}} I(X > a|m, r, \varepsilon) f_{M,R,\mathcal{E}}(m, r, \varepsilon)\, dmdrd\varepsilon \tag{1}$$

, where $\lambda(X > a)$ is the annual rate that ground motion, X, exceeds the target ground motion intensity, a, e.g., peak ground acceleration. ν is the annual rate of earthquake occurrence with magnitude greater than $m_{\min}$ from the source, M is the earthquake magnitude, $m_{\min}$ and $m_{\max}$ are minimum and maximum magnitudes considered for the source, R is the source-to-site distance, $r_{\min}$ and $r_{\max}$ are minimum and maximum source-site distances, $\mathcal{E}$ is a standard normal random variable for generating earthquake ground motion, $\varepsilon_{\min}$ and $\varepsilon_{\max}$ are $\mathcal{E}$'s minimum and maximum values for PSHA computations (generally, $\varepsilon_{\max} \geq 6$ and $\varepsilon_{\min} \leq -6$; Bommer and Abrahamson (2006)), $f_{M,R,\mathcal{E}}(m, r, \varepsilon)$ is joint probability density function (PDF) of M, R, and $\mathcal{E}$, $I(X > a|m, r, \varepsilon)$ is the indicator function that takes 1 when $X > a$, otherwise, 0. The ground motion X given M, R, and $\mathcal{E}$ is generally calculated using ground motion models (Bozorgnia et al., 2014; Goulet et al., 2021). The models usually assume the log-normal distribution for the ground motion given explanatory variables such as M and R. Naturally, these models provide the mean and standard deviation of logarithmic ground motion. Thus, the random ground motion is calculated as:

$$\log X = \mu(M, R) + \mathcal{E}\sigma(M, R) \tag{2}$$

, where μ and σ are the mean and standard deviation of logarithmic earthquake ground motion.

If we assume that the ground motion random variable $\mathcal{E}$ is independent with respect to the M and R (McGuire, 1995), Eq. (1) can be modified as

$$\lambda(X > a) = \nu \int_{\varepsilon_{\min}}^{\varepsilon_{\max}} \int_{r_{\min}}^{r_{\max}} \int_{m_{\min}}^{m_{\max}} I(x > a|m, r, \varepsilon) f_{\mathcal{E}}(\varepsilon) f_{R|M}(r|m) f_M(m)\, dmdrd\varepsilon \tag{3}$$

, where $f_M(m)$, $f_{R|M}(r|m)$, $f_{\mathcal{E}}(\varepsilon)$ are PDF of M, R given M, and $\mathcal{E}$. Under the point source assumption, the distance R and magnitude M become independent random variables. Thus, the seismic hazard is given by

$$\lambda(X > a) = \nu \int_{\varepsilon_{\min}}^{\varepsilon_{\max}} \int_{r_{\min}}^{r_{\max}} \int_{m_{\min}}^{m_{\max}} I(x > a|m, r, \varepsilon) f_{\mathcal{E}}(\varepsilon) f_R(r) f_M(m)\, dmdrd\varepsilon \tag{4}$$

The total seismic hazard from multiple seismic sources (e.g., different faults) is the sum of each, $\Lambda(X > a) = \sum_{i=1}^{n_s} \lambda_i(X > a)$, where $\Lambda(X > a)$ is the total annual rate of exceedance of ground motion, a, i is index for seismic sources, and n_s is the total number of seismic sources. Under the assumption of the Poisson process, the annual probability of exceedance can be converted from the annual rate of exceedance by $1 - e^{-\Lambda(X>a)}$.

Hazard disaggregation

We can also disaggregate the hazard to better understand the earthquakes that contribute most to the hazard. Disaggregation is also used to select the input seismic records and conduct non-linear time-history analyses for the design of many critical buildings (Bazzurro and Cornell, 1999; U. S. Nuclear Regulatory Commission, 2007). Mathematically, disaggregation of the hazard is the joint probability distribution of the M, R, and $\mathcal{E}$ conditional on different levels of hazards a to quantify the contributions of each component. The disaggregation of PSHA can be formulated using Bayes' theorem as

$$\begin{aligned} P(M,R,\mathcal{E}|X>a) &= \frac{P(X>a\cap M,R,\mathcal{E})}{P(X>a)} \\ &= \frac{I(X>a|M,R,\mathcal{E})P(M,R,\mathcal{E})}{\sum_M\sum_R\sum_{\mathcal{E}} I(X>a|M,R,\mathcal{E})P(M,R,\mathcal{E})} \end{aligned} \tag{5}$$

, where $P(X>a|M,R,\mathcal{E})$ is the probability of ground motion X is greater than a given M, R, and $\mathcal{E}$, $P(M,R,\mathcal{E})$ is joint probability of M, R, and $\mathcal{E}$, and $P(X>a)$ is the total probability that the ground motion is greater than a, which is $\sum_M\sum_R\sum_{\mathcal{E}} P(X>a|M,R,\mathcal{E})P(M,R,\mathcal{E})$. Note that $P(X>a|M,R,\mathcal{E})$ can be expressed as an indicator function, $I(X>a|m,r,\varepsilon)$, because the probability of ground motion X greater than a can only be 1 or 0 given m, r, and ε (see Eq. (2)).

By replacing probability mass function, $P(M,R,\mathcal{E})$, with probability density function, $f_{M,R,\mathcal{E}}(m,r,\varepsilon)$, and changing the summation into integration, Eq. (5) can be expressed as:

$$f(m,r,\varepsilon|X>a) = \frac{I(X>a|m,r,\varepsilon)f_{M,R,\mathcal{E}}(m,r,\varepsilon)}{\iiint I(X>a|m,r,\varepsilon)f_{M,R,\mathcal{E}}(m,r,\varepsilon)dmdrd\varepsilon} \tag{6}$$

By Eq. (1), the denominator of Eq. (6) equals λ/ν. Thus,

$$f(m,r,\varepsilon|X>a) = \nu\cdot\frac{I(X>a|m,r,\varepsilon)f_{M,R,\mathcal{E}}(m,r,\varepsilon)}{\lambda} \tag{7}$$

CURRENT NUMERICAL SOLUTIONS

The Riemann Sum This method computes PSHA curves by summing the areas of partitioned (m, r, ε) cuboids. The Riemann Sum for Eq. (1) can be expressed as:

$$\lambda(X>a) = \nu\sum_{k=1}^{N_\varepsilon}\sum_{j=1}^{N_r}\sum_{i=1}^{N_m} I(x>a|m_i,r_j,\varepsilon_k)\, f_{M,R,\mathcal{E}}(m_i,r_j,\varepsilon_k)\Delta m\Delta r\Delta\varepsilon \tag{8}$$

, where Δm, Δr, and $\Delta\varepsilon$ are grid step size for Riemann Sum, N_m, N_r, and N_ε are the total number of grids, satisfying $N_x\Delta x$ = $x_{\max}$ - x_{min}, where $x = \{m, r, \varepsilon\}$. Note that $f_{M,R,\mathcal{E}}(m_i,r_j,\varepsilon_k)\Delta m\Delta r\Delta\varepsilon$ is equivalent to the probability at (m, r, ε) such that $|m-m_i|<\Delta m/2$, $|r-r_j|<\Delta r/2$, and $|\varepsilon-\varepsilon_k|<\Delta\varepsilon/2$. The accuracy of the Riemann Sum depends on the grid size. Utilizing finer grids enhances the accuracy of the summation. However, the computation time is inversely proportional to the grid step

TABLE 1
Comparison of time complexity of various PSHA algorithms

Algorithm	N_m	N_r	N_ε	N_s	N_a
Riemann Sum	N	N	N (1*)	-	1
Conventional MC	1	1	1	N	1
IS MC	1	1	1	N	1
VEGAS AIS (this study)	1	1	1	N	N ($< N^\dagger$)

N_m, the number of magnitude grids; N_r, the number of distance grids; N_ε, the number of ε grids; N_s, the number of (m, r, ε) samples; N_a, the number of ground motion intensity of interest (e.g., 0.1 g)
* when Eq. (26) is used
† when "smart" AIS is used

size and thus proportional to the number of grids. For three-dimensional PSHA summation, the computation time scales with $N_m \times N_r \times N_\varepsilon$ (Table 1). Notably, since the distance PDF ($f_R(r)$) cannot be analytically determined in practice, integration often extends over latitude (ϕ), longitude (ψ), and depth (z), increasing the dimensions from three (m, r, ε) to five (m, ϕ, ψ, z, ε). Therefore, the Riemann Sum for seismic hazard becomes even more computationally intensive, a phenomenon known as "the curse of dimensionality" due to the exponential increase in computation time with the number of dimensions (Novak and Ritter, 1997).

Conventional Monte-Carlo (MC) This method simulates many synthetic earthquake ground motions and calculates PSHA by assessing the frequency with which ground motion intensities exceed a certain threshold. MC PSHA is computed as

$$\begin{aligned}\hat{\lambda}(X > a) &= \frac{\nu}{N_s}\sum_{i=1}^{N_s} I(X_i > a|M_i, R_i, \mathcal{E}_i) \\ &= \frac{1}{T}\sum_{i=1}^{N_s} I(X_i > a|M_i, R_i, \mathcal{E}_i)\end{aligned} \tag{9}$$

, where X_i denotes the simulated ground motions, and N_s is the total number of samples. M_i, R_i, $\mathcal{E}_i$ are random samples from $f_{M,R,\mathcal{E}}(m, r, \varepsilon)$, T represents the equivalent catalog duration equal to N_s/ν. MC PSHA is unbiased, i.e., the expectation of $\hat{\lambda}(X > a)$ is the same as λ, and the variance of $\hat{\lambda}$, VAR$[\hat{\lambda}]$, is $(\nu\lambda - \lambda^2)/N_s$ (see Appendix A for derivation). Note that VAR$[\hat{\lambda}]$ is always positive since $\nu \geq \lambda$. The coefficient of variation, COV, a widely used metric to estimate relative uncertainty with respect to the mean, is:

$$COV = \frac{\sqrt{\mathrm{VAR}[\hat{\lambda}]}}{E[\hat{\lambda}]} = \sqrt{\frac{\nu - \lambda}{N_s\lambda}} \tag{10}$$

COV is inversely proportional to the square root of the number of MC samples (N_s), indicating that increasing N_s naturally improves the estimate's accuracy. The target exceedance rate, λ, also affects the MC accuracy. The lower λ leads to poor accuracy with fixed N_s and ν. Thus, a sufficiently long earthquake catalog is required to accurately estimate the event from a long return period. It is also notable that COV is increasing with earthquake occurrence rate, ν, indicating that MC PSHA is a more challenging task in regions with higher earthquake activity. This can also be explained intuitively. Regions with high seismic activity experience more earthquakes per year than less active areas; therefore, when calculating the ground motion exceedance probability over the same period, more earthquakes need to be considered in these active regions.

In MC PSHA, each realization of the ground motion can be leveraged to compute hazard estimates at different intensity levels. An advantage of MC PSHA is that the computational time is dependent on the number of samples N_s, circumventing the inherent dimensionality problem in Riemann Sum (Table 1). In other words, the computation time of MC simulation is independent of the number of grids (N_m, N_r, and N_ε in Eq. (8)). Therefore, we could utilize fine joint probability mass functions for more precise hazard estimation without an increase in computational burden. If closed-form probability density functions are available, PSHA can be implemented without approximated discretization.

Conventional MC faces extreme computational challenges for low probabilities because the number of samples required to achieve low COVs dramatically increases. We can compute the required number of samples by rearranging Eq. (10):

$$N_s = \frac{1}{(COV)^2} \times \frac{\nu - \lambda}{\lambda} \tag{11}$$

For small λ, i.e., $\nu >> \lambda$, the Eq. (11) can be approximated as $N_s \sim \frac{1}{(COV)^2} \times \frac{\nu}{\lambda}$. To demonstrate conventional MC's extreme computational demands, we can calculate N_s for a target annual exceedance rate, λ, of 10^{-4} per year and an annual earthquake rate $\nu = 1/\text{yr}$, which is typical values in PSHA practice (Coppersmith et al., 2014). From Eq. (11), we need $N \sim 10^8$ to achieve COV = 1%.

Importance Sampling (IS) Integration

IS is a generalization of MC theory. Consider a random variable X that follows a probability density function, $f_X(x)$. The expected value of a function $u(x)$, denoted as S, is defined by

$$S = \int u(x) f_X(x) dx \tag{12}$$

The MC estimate is

$$\hat{S} = \frac{1}{N_s} \sum_{i=1}^{N_s} u(X_i) \tag{13}$$

, where X_i is sampled from $f_X(x)$.

By introducing an arbitrary probability density function, $q_X(x)$, Eq. (12) can be equivalently expressed as

$$S = \int u(x) \frac{f_X(x)}{q_X(x)} q_X(x) dx \tag{14}$$

We restrict the integration range in Eq. (14) where $f_X(x) \neq 0$ because x such that $f_X(x) = 0$ does not contribute to the integration. Then, $q_X(x)$ can be any distribution with nonzero density in the integration range. Eq. (14) provides important implications in MC estimation. We can get the solution to Eq. (12) by estimating the expected value of $u(x) f_X(x)/q_X(x)$ where x follows the distribution $q_X(x)$. This approach is highly useful in numerical integration, especially when sampling from $f_X(x)$ is challenging or the population of $f_X(x)$ is extremely low in the region of importance. For example, the exceedance rate of PGA greater than 1 g is mostly contributed by the ground motion samples from large magnitude (M) earthquakes occurred at close distance (R) with large $\mathcal{E}$, which all typically correspond to the low probability region.

The IS MC estimate is:

$$\hat{S} = \frac{1}{N_s} \sum_{i=1}^{N_s} u(X_i) \frac{f_X(X_i)}{q_X(X_i)} \tag{15}$$

, where X_is are sampled from $q_X(x)$, the proposed (or new) IS sampling density function. If $q_X(x)$ is equal to the original distribution, $f_X(x)$, Eq. (15) simplifies to the conventional Monte-Carlo (Eq. (13)). The ratio $f_X(x)/q_X(x)$, known as the importance weight (w_i), adjusts for the change in sampling distribution.

IS PSHA Researchers have applied IS to PSHA using different sampling functions (Jayaram and Baker, 2010; Rahimi and Mahsuli, 2019). For IS PSHA, Eq. (1) can be reformulated by introducing a new sampling joint density function, $q_{M,R,\mathcal{E}}(m,r,\varepsilon)$ as follows

$$\lambda(X>a)=\nu\int_{\varepsilon_{\min}}^{\varepsilon_{\max}}\int_{r_{\min}}^{r_{\max}}\int_{m_{\min}}^{m_{\max}} I(x>a|m,r,e)\frac{f_{M,R,\mathcal{E}}(m,r,\varepsilon)}{q_{M,R,\mathcal{E}}(m,r,\varepsilon)}q_{M,R,\mathcal{E}}(m,r,\varepsilon)\,dmdrd\varepsilon \tag{16}$$

The IS MC estimator of equation (16) is

$$\hat{\lambda}(X>a)=\frac{\nu}{N_s}\sum_{i=1}^{N_s} I(X_i>a|M_i,R_i,E_i)\frac{f_{M,R,\mathcal{E}}(M_i,R_i,E_i)}{q_{M,R,\mathcal{E}}(M_i,R_i,E_i)}$$

The mean of IS estimator $\hat{\lambda}$ is also unbiased like conventional MC, i.e., $E_q[\hat{\lambda}]=\lambda$ (see Appendix B for derivation). Also, the variance of the IS PSHA estimates with respect to the true λ is given by

$$\mathrm{VAR}[\hat{\lambda}]=\frac{1}{N_s}\left(\nu^2 E_q\left[\left(I(X_i>a|M_i,R_i,\mathcal{E}_i)\frac{f_{M,R,\mathcal{E}}(M_i,R_i,\mathcal{E}_i)}{q_{M,R,\mathcal{E}}(M_i,R_i,\mathcal{E}_i)}\right)^2\right]-\lambda^2\right) \tag{17}$$

(see Appendix B for derivation). Hence, the COV of IS PSHA estimate can be expressed as

$$COV=\sqrt{\frac{\nu^2 E_q\left[\left(I(X_i>a|M_i,R_i,\mathcal{E}_i)\frac{f_{M,R,\mathcal{E}}(M_i,R_i,\mathcal{E}_i)}{q_{M,R,\mathcal{E}}(M_i,R_i,\mathcal{E}_i)}\right)^2\right]-\lambda^2}{N_s\lambda^2}} \tag{18}$$

Equivalency of optimal IS density and hazard disaggregation

From Eq. (17), we can specifically choose a new sampling density $q^*_{M,R,\mathcal{E}}$ that makes VAR[$\hat{\lambda}$]=0,

$$q^*_{M,R,\mathcal{E}}=\nu\frac{I(X_i>a|M_i,R_i,\mathcal{E}_i)f_{M,R,\mathcal{E}}(M_i,R_i,\mathcal{E}_i)}{\lambda} \tag{19}$$

Using $q^*_{M,R,\mathcal{E}}$, we could compute the true hazard, λ, with only one MC sample because IS MC is unbiased and the variance is zero. We call q^* the optimal IS density for PSHA calculation.

We note that Eq. (19) is exactly the same as Eq. (7), indicating that the optimal density, q^*, is identical to the hazard disaggregation. That is, if we find q^*, we are able to not only dramatically enhance the computational efficiency of seismic hazard estimation but also obtain the hazard disaggregation distributions as a by-product.

In fact, we can also see this profound relationship between the hazard and disaggregation estimates by rearranging Eq. (7):

$$\lambda\equiv\nu\cdot\frac{I(X>a|m,r,\varepsilon)f_{M,R,\mathcal{E}}(m,r,\varepsilon)}{f(m,r,\varepsilon|X>a)}$$

Because this identity holds for any values of (m, r, ε), we can obtain the hazard at ground motion level, a, with any (m, r, ε) triplet if we know $f(m, r, \varepsilon | X > a)$. The term $f_{M,R,\mathcal{E}}(m, r, \varepsilon)/f(m, r, \varepsilon | X > a)$ can be interpreted as the importance weight of IS, and $f(m, r, \varepsilon | X > a)$, the hazard disaggregation, is the optimal density. Note that this identity also holds in the "equal" hazard case, where the indicator function $I(X > a)$ becomes $I(X = a)$ (or $I(a_1 < X \leq a_2)$).

The disaggregation can be computationally expensive in memory usage. In Riemann Sum, we must save each sum element in memory and allocate those elements into appropriate disaggregation bins, though the elements are readily computed in the hazard computation process. Also, in conventional MC, we should save the long synthetic ground motion catalog with the corresponding (m, r, ε) triplet to allocate those into the proper bins. These operations necessitate additional computational memory and time. Therefore, finding q^* could bring significant benefits by simultaneously producing disaggregation and hazard curves. However, finding q^* is not trivial in current implementations of PSHA because $I(X_i > a | M_i, R_i, E_i)$ and λ in Eq. (19) are unknowns. Thus, we propose a new PSHA computation method to find it.

ADAPTIVE IMPORTANCE SAMPLING PSHA

In "adaptive" importance sampling (AIS), we iteratively train the IS density to find the optimal one (q^*) by exploring important regions to compute $I(X_i > a | M_i, R_i, E_i)$ and λ with a reduced number of MC samples. Regardless of the algorithm used, AIS must balance different factors in determining how many samples (N_s) should be used to train optimal IS density. If we use a small number of samples to update the sampling distribution, we will not explore the important regions effectively, making the number of iterations increase. On the other hand, many samples can reduce the number of iterations, however, it imposes large computational demands per iteration, making it computationally ineffective. Therefore, it is important to select appropriate algorithms that effectively find the important regions and converge fast.

VEGAS Formulation for PSHA VEGAS is a non-parametric AIS algorithm that iteratively identifies the optimal proposal density, q^* (Lepage, 1978, 2021). The algorithm has been developed and widely used in computational physics (Kersevan and Richter-Was, 2013; Alwall et al., 2014), and is currently applied to chemistry, astrophysics, finance, and medical statistics (Campolieti and Makarov, 2007; Garberoglio and Harvey, 2011; Ray et al., 2011; Sanders, 2014).

The VEGAS algorithm is conceptually straightforward and is recognized for its rapid convergence, especially when the random variables involved are independent (Lepage, 1978, 2021). In PSHA, the variable $\mathcal{E}$ is always considered an independent variable (Eq. (3)). Additionally, the variables M and R are also treated as independent under point source assumption (Eq. (4)). Notice, however, that when the finite-fault rupture model, in which the rupture dimension changes with magnitude, is adopted, M and R can be correlated, and the distribution of R is conditional on the magnitude M. Also, note that the estimate remains unbiased in this case, because its calculation is still within the IS framework.

In three-dimensional integration, which is the case of PSHA, VEGAS employs N^3 cuboids that are independently partitioned. The probability assigned to each cuboid and the total number of partitioned cuboids (N^3) is preserved across the iteration steps. However, the IS sampling density changes because the algorithm updates the cuboid's size depending on its contribution to the integration. If a cuboid's contribution is low, its size grows in the next step, lowering its probability density. Conversely, when a cuboid's contribution is high, it shrinks in the following step, elevating the probability density. Ideally, when every cuboid's contribution to the integration becomes identical, we find the proposed optimal density, q^*, and the algorithm is terminated. The framework to find optimal IS densities for PSHA using the VEGAS algorithm is illustrated with a simple point seismic source example in the following paragraphs.

First, we adopt an independently distributed joint probability function as IS density, significantly improving the efficiency of the iterative updating process in multi-dimensional PSHA integration. Thus, $q_{M,R,\mathcal{E}}(m,r,\varepsilon) = q_M(m)q_R(r)q_\mathcal{E}(\varepsilon)$. Then, the integration ranges for each random variable—M, R, and $\mathcal{E}$—are divided into N grids with the same volume. This division is designed to generate cuboids of constant probability:

$$\begin{aligned} &M : m_{i-1} \le M < m_i \ (i = 0, 1, 2, .., N), \Delta m_i = m_i - m_{i-1} \\ &R : r_{j-1} \le R < r_j \ (j = 0, 1, 2, .., N), \Delta r_j = r_j - r_{j-1} \\ &\mathcal{E} : \varepsilon_{k-1} \le \mathcal{E} < \varepsilon_k \ (k = 0, 1, 2, .., N), \Delta \varepsilon_k = \varepsilon_k - \varepsilon_{k-1} \end{aligned} \tag{20}$$

The number of grids, N, is chosen to be 50 as suggested by Lepage (1978) and because we consider this value makes grids sufficiently fine to capture the actual distribution of the optimal density q^*. The probability for each cuboid from Eq. (20) is set to $1/N^3$ to ensure that the initial IS density function is uniformly distributed across the entire domain. As a result, the initial probability density $q^{(0)}$ for a specific cuboid is

$$\begin{aligned} q^{(0)}(m_{i-1} \le M < m_i,\ r_{j-1} \le R < r_j,\ \varepsilon_{k-1} \le \mathcal{E} < \varepsilon_k) &= q_M^{(0)}(M)\, q_R^{(0)}(R)\, q_\mathcal{E}^{(0)}(\mathcal{E}) \\ &= \frac{1}{N\Delta m_i}\frac{1}{N\Delta r_j}\frac{1}{N\Delta \varepsilon_k} \end{aligned}$$

Figure 1 illustrates an example of initial partitioning when N=10. The gray dots in the figure show an example of MC samples from this initial q^0. Note that for easier visualization and understanding, Figure 1 illustrates an example in m-ε, the two-dimensional space, and not the three-dimensional m, r, and ε space.

We update q using MC samples $(M, R, \mathcal{E})$ to ultimately make it converge to q^* (Eq. (19)). As mentioned earlier, the size of each cuboid is subject to change while the probability of each cuboid remains constant, i.e., probability density changes. This adjustment is facilitated through a "subdivision-and-restoration" process (Lepage, 1978). In this process, each VEGAS grid is first subdivided into sub-grids given the total number of sub-grids (N_{subgrid}). Since N_{subgrid} should be sufficiently larger than N to iterate the IS density effectively, we chose N_{subgrid} to be 10,000, which is 200 times greater than N (=50). At each

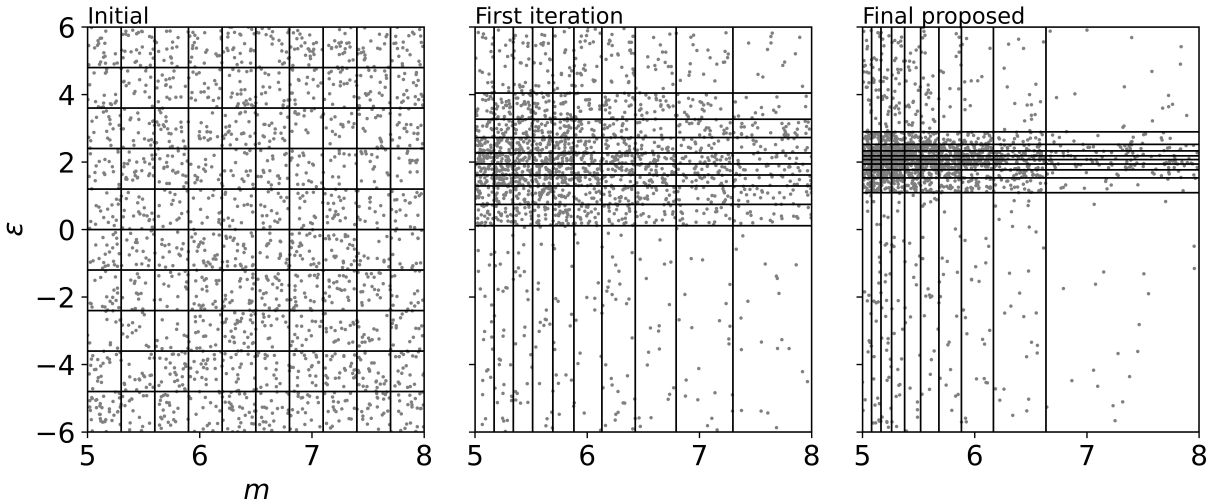

Figure 1. VEGAS iterations of IS density in our AIS PSHA framework. Example for PSHA at PGA = 0.5 g when the site is located 10 km away from a point seismic source ($m_{\min}$ = 5.0, $m_{\max}$ = 8.0, b-value = 1.0, ν = 1.0/yr, Ground Motion Model (GMM) = Sadigh et al. (1997)). The total number of MC samples is 2,000, and the number of grids per axis is 10, constituting a total of 100 rectangles (cuboids in actual three-dimensional PSHA integration). The vertical and horizontal black solid lines are boundaries of the m and ε rectangles, and gray dots are the MC samples. Starting from the initial same-size m and ε rectangles, their sizes are adjusted depending on the contribution of each rectangle to the hazard. The final proposed structure of the rectangles gives a highly concentrated probability density at $m \sim 5$ and $\varepsilon \sim 2$. Note that the hazard estimates using initialized density, density after the first iteration, and the final proposed density are 0.0417, 0.0413, and 0.0378, while the true solution is 0.0385.

VEGAS grid, the number of sub-grids is proportional to each grid's contribution to the overall integration, d_i:

$$d_i = \frac{\overline{H}_i \Delta x_i}{\sum_i \overline{H}_i \Delta x_i} \tag{21}$$

,where $\overline{H}_i$ in m axis is (Lepage, 1978):

$$\overline{H}_{i,m} = \sqrt{\sum_{m_{i-1}<M<m_i} \frac{H^2(M,R,\mathcal{E};a)}{q_R(R)q_{\mathcal{E}}(\mathcal{E})}} \tag{22}$$

, where $H(M,R,\mathcal{E};a)$ is the integrand of PSHA, $I(X>a|M,R,\mathcal{E})f_{M,R,\mathcal{E}}(M,R,\mathcal{E})$. Intuitively, $\overline{H}_i$ can be considered as the marginalization of the overall contribution of the magnitude dimension within the ith grid. Note that the summation of H^2s in Eq. (22) is done over all the samples which fall within m_{i-1} and m_i and the division by q_R $q_{\mathcal{E}}$ can be considered an adjustment for unevenly distributed R and $\mathcal{E}$ samples to purely capture the magnitude contribution.

Similarly, $\overline{H}_i$ in r and ε axes can be calculated as

$$\overline{H}_{i,r} = \sqrt{\sum_{r_{i-1}<R<r_i} \frac{H^2(M,R,\mathcal{E};a)}{q_M(M)q_{\mathcal{E}}(\mathcal{E})}}$$

$$\overline{H}_{i,\varepsilon} = \sqrt{\sum_{\varepsilon_{i-1}<\mathcal{E}<\varepsilon_i} \frac{H^2(M,R,\mathcal{E};a)}{q_R(R)q_M(M)}}$$

After the sub-division of each VEGAS grid with the numbers proportional to d_i, the total number of grids is restored to the original number, N, by merging N_{subgrid}/N consecutive subgrids. The restored grid is the updated density, $q^{(1)}$. The iterative process described above is repeated until no further changes occur in d_i (Eq. (17)).

In the early iterations, researchers have noticed numerical instabilities due to the relatively poor information on the integrand (Lepage, 1978, 2021). However, researchers have also found effective ways to mitigate it through smoothing (Eq. (23)) and damping (Eq. (24)). The smoothed and damped contributions at ith VEGAS grid, d_s and d_d, are calculated as:

$$d_s := \frac{1}{\sum d_i} \times \begin{cases} (7d_i + d_{i+1})/8 & \text{if } i = 0 \\ (d_{i-1} + 6d_i + d_{i+1})/8 & \text{if } i = 1, 2, ..., N-1 \\ (d_{i-1} + 7d_i)/8 & \text{if } i = N \end{cases} \tag{23}$$

$$d_d := \left(\frac{1 - d_s}{\ln(1/d_s)} \right)^{\alpha} \tag{24}$$

, where α is learning rate. We used α as 1.0 as suggested by Lepage (2021). Through numerical experimenting, we observed this value allowed most of the PSHA integration to converge within three iterations without causing any numerical instabilities.

This VEGAS iteration process is illustrated in Figure 1. The sizes of the grids are shrunk at $5 < m < 6$ and $\varepsilon \sim 2$, indicating that the high contributions to the hazard on this range (d_i) in contrast to other less important regions, e.g., at $m > 6.5$ and $\varepsilon < 1$. Note that the probability of each grid is preserved so that the number of MC samples inside each grid is almost the same regardless of the grid size. The final proposed density exhibits features that are expected based on intuition. First, the low contribution of ε less than 0 is understandable. This is because the simulated ground motion intensity, using Sadigh et al. (1997), never exceeds the target ground motion of 0.5 g at any magnitude, even at $m = 8.0$, when ε is less than 0.1. In addition, the strong contribution of $m \sim 5$ and $\varepsilon \sim 2.2$ to the integration makes sense because the simulated ground motion intensity exceeds the target ground motion of 0.5 g when m and ε reach 5 and 2.2, respectively. The decreasing trend of contribution beyond $m \sim 5$ and $\varepsilon \sim 2.2$ can be interpreted as the exponential decay in the probability of m and ε. This result for a simple PSHA example implies that the proposed algorithm can be utilized for more complex PSHA integration.

NUMERICAL EXAMPLES

We tested our proposed AIS PSHA using five numerical examples. For examples 1 to 3, we utilized benchmark problem sets 1.11 and 2.1 from the PEER PSHA code verification project (Hale et al., 2018) to validate the method against the verified

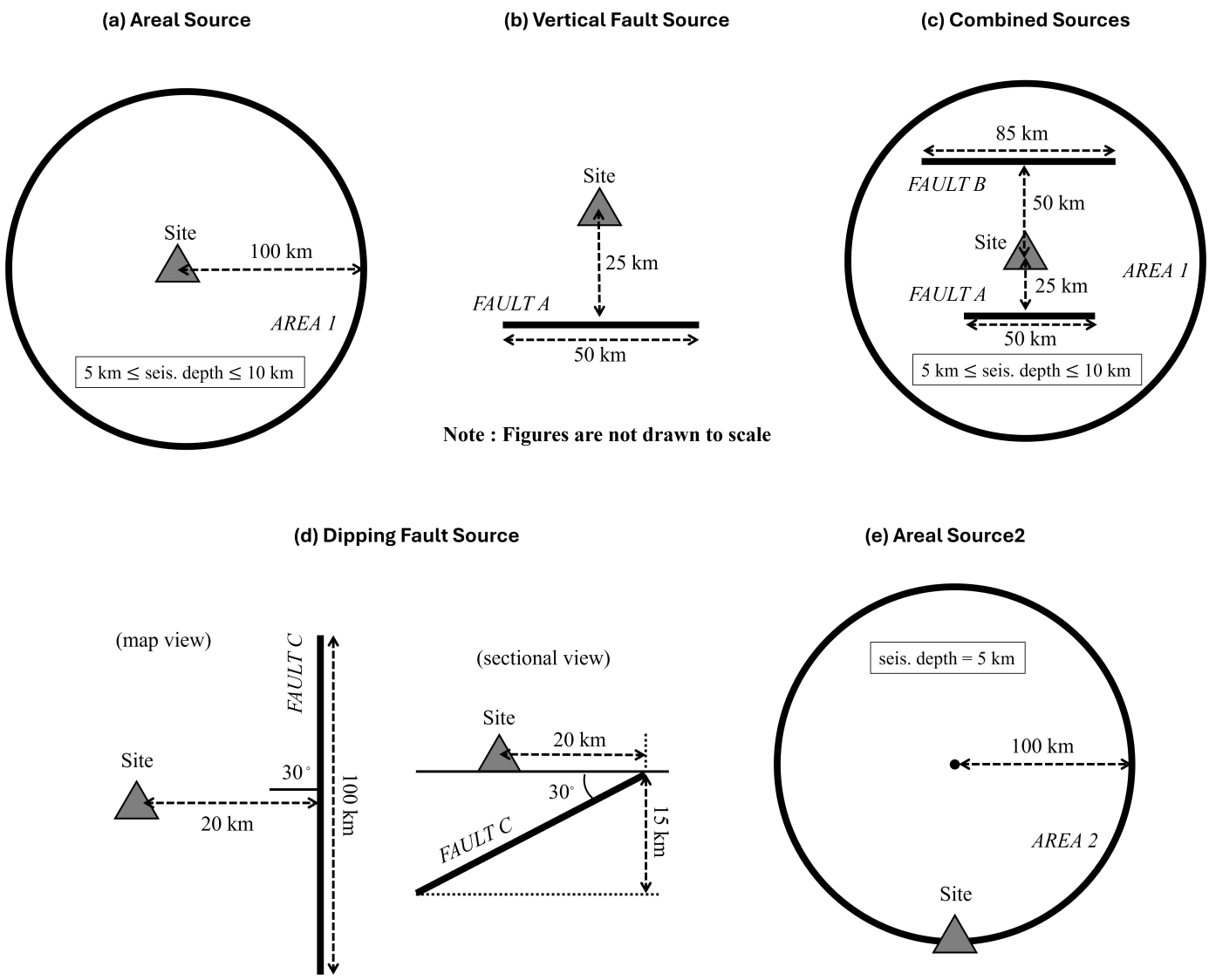

Figure 2. Seismic source geometry for the numerical examples to test our AIS PSHA framework.

benchmark PSHA curves (Figure 2 (a)-(c)). The examples encompass various seismic source types such as area, fault, and combined sources. In Example 4, dipping fault is introduced with widely used model parameters common in PSHA practice (Figure 2 (d)). For these Examples, the computational efficiency of AIS PSHA is compared with pre-existing numerical solutions such as Riemann Sum, conventional MC, and IS with uniform sampling distribution (Jayaram and Baker, 2010). For the accurate Riemann Sum, we followed the procedure of Hale et al. (2018). Finally, in Example 5, we introduced an advanced version of AIS, termed "smart" AIS, and tested it against a "smart" Riemann Sum variant that uses a strategic grid spacing to solve problem set 1.10 of Hale et al. (2018) (Figure 2 (e)).

For all the examples, the probability of exceedance at eighteen ground motions (PGA), 0.001, 0.01, 0.05, 0.1, 0.15, 0.2, 0.3, 0.35, 0.4, 0.45, 0.5, 0.55, 0.6, 0.7, 0.8, 0.9, and 1.0 g, are estimated. Each example's model parameters are detailed in Table S1, and their benchmark hazard curves are shown in Figure 3. The analyses were conducted in Python 3.11 on an Intel Core i7-13700 2100 MHz processor with 64GB RAM.

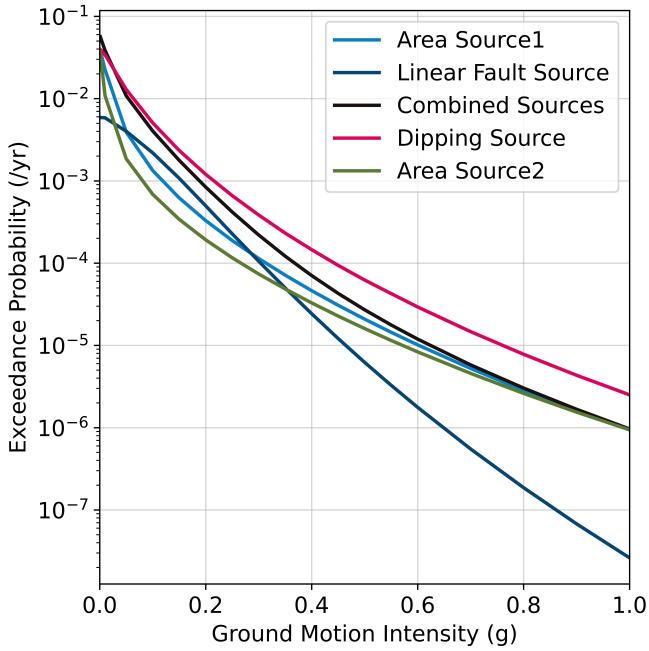

Figure 3. Benchmark PSHA curves for area source 1, linear fault source, combined sources, dipping source, and areal source 2. The benchmark curves are obtained from either Hale et al. (2018) (for areal source 1, combined sources, and areal source 2) or calculation by the authors (linear fault source and dipping source).

Example 1: Areal source

We consider the circular area source with the site at the circle's center (Figure 2). We solved the PSHA using Riemann Sum, conventional MC, uniform IS, and AIS, and show their performance (Figure 4; see Figure S2 for the results on the other ground motion levels). Our numerical experiments show that computational times and COV ("accuracy") are linearly correlated in logarithmic scale, in agreement with the theory (Eq. (11)).

While the computation time and COV vary depending on the target ground motion of interest, our results show our AIS PSHA generally outperforms the other numerical techniques. At a low target ground motion of 0.05g, the computation time to achieve a 1 % COV, i.e., 95 % of the hazard estimates being within 2% error range, is 0.04 seconds for AIS, while it takes 0.20 and 0.39 seconds for conventional MC and IS estimates, respectively, indicating AIS is 4.4 and 8.7 times faster. The computational efficiency becomes extreme at higher ground motions. At 0.3 g, which corresponds to the exceedance probability of $\sim 10^{-4}$/yr, the computation time to achieve 1 % COV is estimated to be 0.06 seconds for AIS, while it takes 7.14 and 1.81 seconds for conventional MC and IS estimates. In this case, AIS is 111 and 28 times faster than conventional MC and IS, respectively. At the extreme ground motion, 1.0 g, the computation time to achieve 1 % COV is estimated to be 0.09 seconds for AIS, while it takes 633 and 6.53 seconds for conventional MC and IS estimates. In this case, AIS is 7,128 and 73 times faster than conventional MC and IS, respectively. Also, for the 1 % COV case, AIS is $\sim 3.7 \times 10^4$ faster than Riemann Sum. We also note that AIS outperforms IS in all ground motion ranges by a factor of 12 to 73 to achieve a 1 % COV. However, this performance is not always guaranteed because AIS takes t times more computational time than IS with the same N due to the t iterations

to find the optimal IS density. Thus, our findings imply that AIS PSHA with the VEGAS algorithm can find (close to) optimal IS density quickly.

It is also noteworthy that with the fixed number of samples (i.e., constant computational burden), AIS's estimation accuracy is quite similar across different target ground motions, while conventional MC's accuracy decreases sharply for higher ground motions (Figure 5). According to Eq. (10), COV of MC hazard estimates for the ground motion corresponding to 10^{-6}/year will increase to 10% if it initially was 1 % for the ground motion corresponding to 10^{-4}/year. From our numerical experiments, we found errors grow from 0.54 to 5.60 % with $N_s = 10^7$ MC samples for these ground motions (0.3g and 1.0g). In contrast, for a similar computation time, we found AIS had errors ranging from 0.51 to 0.67 % for these quite different ground motion levels (Figure 5).

This finding is key for PSHA as the computational bottleneck is at the highest ground motion intensity. Using conventional MC PSHA, the hazard analyst has no choice but to largely increase the number of samples to estimate hazard accurately at high ground motions even though such a large number would not be necessary for low ground motions. This makes the conventional MC highly inefficient, and consequently, the efficiency of the conventional MC for lower ground motions cannot be considered a real advantage for PSHA. AIS PSHA overcomes this problem by adopting different optimal densities at different ground motion intensities, making the computational burden to achieve the similar estimation error almost flat for any ground motion intensity, as shown in Figure S3. We observed that that AIS PSHA achieves 2.5 % and 1.0 % COV with $N_s \sim 10{,}000$ and 50,000, respectively (Figure S3).

Another key advantage of our proposed AIS PSHA is the co-production of disaggregation curves at no extra computational cost. From Eq. (19), optimal IS densities are theoretically equivalent to hazard disaggregation. We showed that the benchmark marginal distributions of hazard disaggregation obtained from Riemann Sum closely match the iterated IS density from AIS PSHA (Figure 6; see Figure S4 for the results on the other ground motion levels). We used the Kolmogorov-Smirnov (K-S) D statistic (Kolmogorov, 1933) to quantify their similarities. K-S D statistic measures the maximum difference between two cumulative distribution functions (CDF):

$$D = \max_x |F(x) - Q(x)|$$

, where x is m, r, or ε, $F(x)$ is the marginal CDF of disaggregation result, $Q(x)$ is the CDF of proposed IS density obtained from VEGAS. D is larger for more dissimilar CDFs, with a maximum possible value of one. Conversely, if two CDFs are identical, D is zero. Thus, D close to zero indicates that the two probability distributions are similar. For reference, examples of K-S D statistics are illustrated in Figure S1.

We calculated D for m, r, and ε at all the ground motion intensities (Figure S5). We found the maximum D values for m, r, ε were 0.032, 0.113, and 0.092, respectively, and the minimum values were 0.019, 0.026, and 0.017, indicating a strong resemblance between the two distributions.

We also estimated the differences between the disaggregation's mean values from the proposed IS density and Riemann Sum (Figure S5). Note that the disaggregation distributions and proposed IS densities vary for different ground motion levels. Thus, their mean values also vary. We found the maximum relative differences were 2.5 %, 22.6 %, and 18.5 % for m, r, ε, and the minimum differences were 1.7 %, 1.0 %, and 4.3 %, respectively. Also, the maximum absolute differences were 0.14, 3.9 km, and 0.17 for m, r, ε, and the minimum differences were 0.09, 0.7 km, and 0.0009. The maximum relative difference in distance (r) appears for disaggregation distributions at 0.25 g, where the mean distance obtained from hazard disaggregation is 14.3 km and that from the proposed IS density is 17.5 km. Given that we are typically interested in distance ranges on the order of tens of kilometers (e.g., 0-15 km, 15-25 km, 25-50 km, etc.) rather than a single value (U. S. Nuclear Regulatory Commission, 2007), this difference is not crucial in determining the controlling earthquake for critical infrastructures. In addition, IS densities still show small K-S D statistics and their mode almost matches each other, as shown in Figure 6.

Example 2: Fault source

We consider a 50 km-length vertical fault 25 km away from the site (Figure 2 (b)). We adopted a finite-dimension rupture model, which results in a distance distribution dependent on magnitude. We found this dependency diminishes the performance of VEGAS AIS because the VEGAS algorithm assumes the independently distributed random variables. For example, for a ground motion intensity of 0.05 g, AIS is slower than conventional MC (Figure S6), while AIS outperformed conventional MC at the same ground motion intensity when point source assumption was made, as seen earlier. However, as the ground motion intensity increases, the computational gap between the two methods becomes smaller rapidly and closes at 0.2g. For higher ground motions, AIS outperforms conventional MC. At 0.3 g, corresponding to $\sim 10^{-4}$ exceedance probability, for a 1% COV, AIS, IS, and conventional MC take 0.25, 71, and 0.43 seconds, respectively, i.e., AIS MC is 277 and 1.7 times faster. At more extreme ground motion (1.0 g), AIS, IS, and conventional MC take 0.25, 96, and 4,294 seconds, respectively, i.e., AIS is 390 and 17,448 times faster (Figure 4; see Figure S6 for the results on the other ground motion levels). We observed that AIS PSHA estimates approximate the true hazard curve at 2.5 % and 1.0 % COV when N_s is $\sim$ 50,000 and 300,000, respectively (Figure S7).

We also compared hazard disaggregation and the iterated IS density (Figure 6; see Figure S8 for the results on the other ground motion levels) and showed they closely match each other even though the distance distribution depends on the magnitude in this case. It is also noteworthy that the iterated IS density can even reproduce complex densities with discontinuities like the large jump within magnitude distribution (for m =6.25). The K-S D statistic and mean difference of the two distributions are also presented in Figure S9. The maximum values of D in m, r, and ε are 0.30, 0.68, and 0.13, respectively, and the minimum values are 0.02, 0.31, and 0.04. We found that the largest discrepancies occur in the magnitude distribution, but errors can be considered negligible as the mean magnitude difference is within 6 % error. We also note considerable discrepancies in the distance distribution shape (see K-S D statistics of Figure S9) as curves with concentrated probabilities

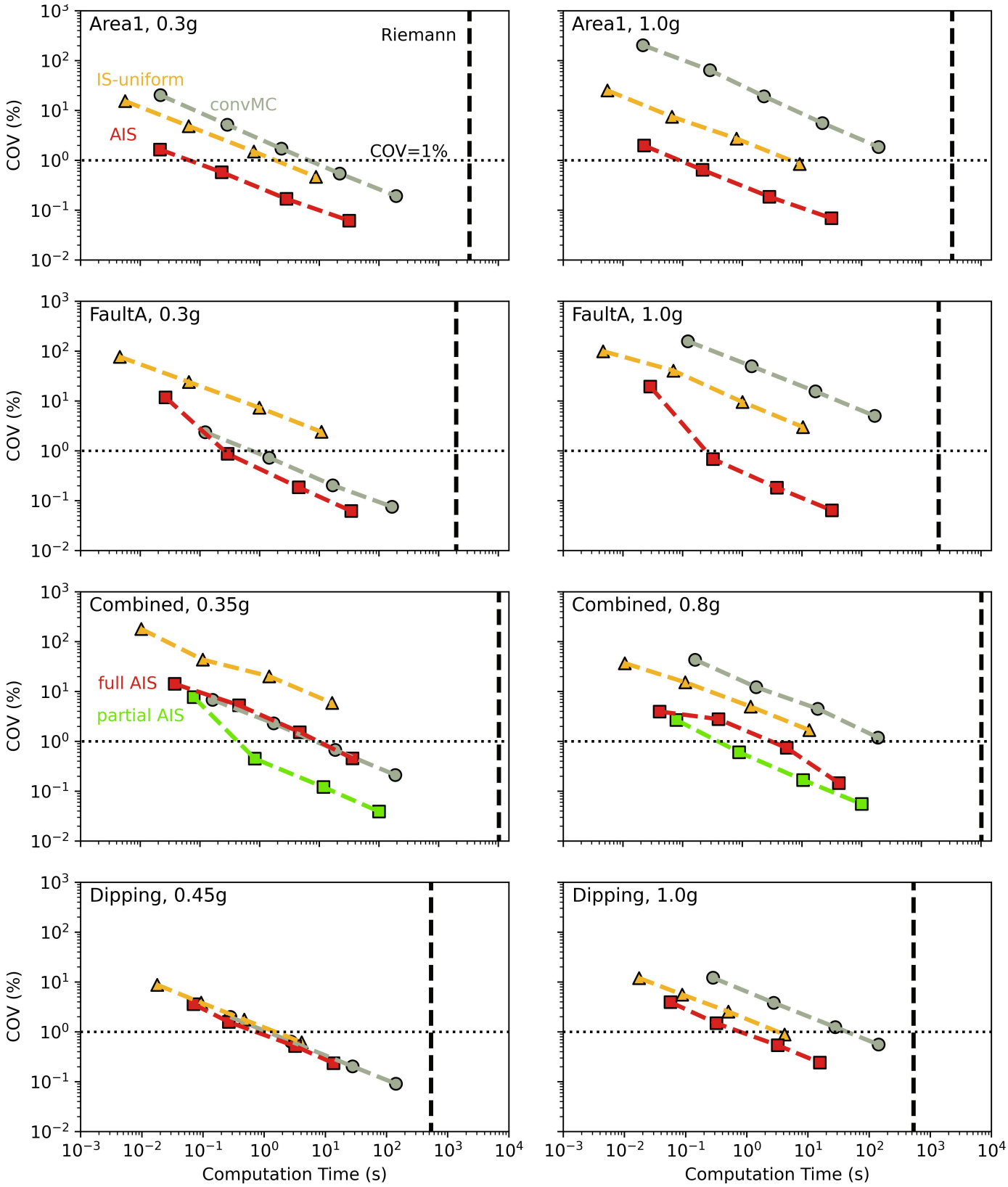

Figure 4. Example 1-4 (Area (Area1), Vertical fault (FaultA), Combined, and Dipping fault (FaultC) sources example): COV as a function of computation time using various PSHA numerical solutions at ground motion intensities that correspond to 10^{-4}/yr: 0.3g, 0.3g, 0.35g, and 0.45g for the area, fault, combined, dipping fault sources, respectively, and extreme ground motion intensities: 1.0g ($\sim 10^{-6}$/yr), 1.0g (2.62×10^{-8}/yr), 0.8g (3.11×10^{-6}/yr), and 1.0g (2.51×10^{-6}/yr) for area, vertical fault, combined, and dipping fault sources, respectively. COV of 1% is denoted as dotted horizontal lines. As the target ground motion increases, the performance of AIS makes a dramatic improvement in terms of both accuracy and computational cost.

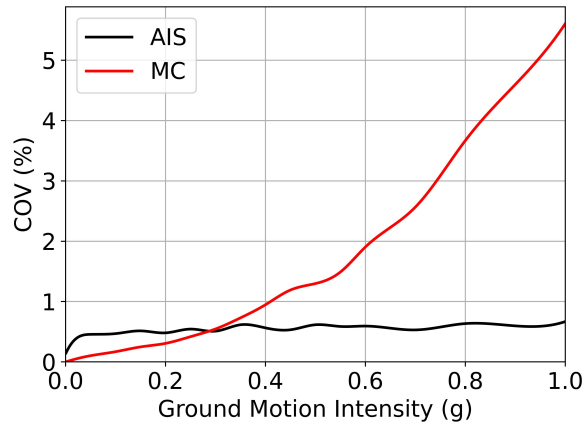

Figure 5. COV of MC estimates with the ground motion for conventional (red) MC ($N_{\text{s, convMC}} = 10^7$) and AIS (black) with the similar computation time. The COV of error exponentially increases with the ground motion in conventional MC, while that of AIS remains constant.

in narrow ranges are harder to estimate for AIS (Figure 6). However, the mean distance is still within a 5 % error range. The ε is generally in good agreement across all ground motion intensities. We observe higher differences at lower ground motion because the mean ε is close to zero. For example, the calculated mean ε at ground motion intensity of 0.01 g is 0.022 and 0.007, which is not a large difference in practice.

The maximum relative differences in mean values were found to be 6.2 %, 5.3 %, and 129 % for m, r, ε, and the minimum differences were 0.006 %, 3.9 %, and 2.2 %, respectively. Note that the 129 % of ε case corresponds to the case where the mean ε is close to zero. The relative difference appears to be slightly higher than the previous areal source example, however, the absolute difference still remains significantly small; the maximum absolute differences were 0.36, 1.3 km, and 0.20 for m, r, ε, and the minimum differences were 0.0004, 1.0 km, and 0.07.

Example 3: Combined sources

In PSHA, we often have multiple seismic sources. We consider one area and two fault sources around the site to represent this case. This application posits a different mathematical problem than the previous two examples because we must introduce an additional variable to formulate AIS.

First, the probability of earthquake occurrence at ith seismic source can be defined as:

$$P(S = i) = \frac{\nu_i}{\sum_{j=1}^{n_s} \nu_j}$$

, where n_s is the number of seismic sources ($n_s = 3$ in this example), and ν_i is the annual earthquake occurrence rate of ith seismic source. Because the discrete random variables cannot be used in AIS, we define a continuous random variable and its corresponding probability density function as

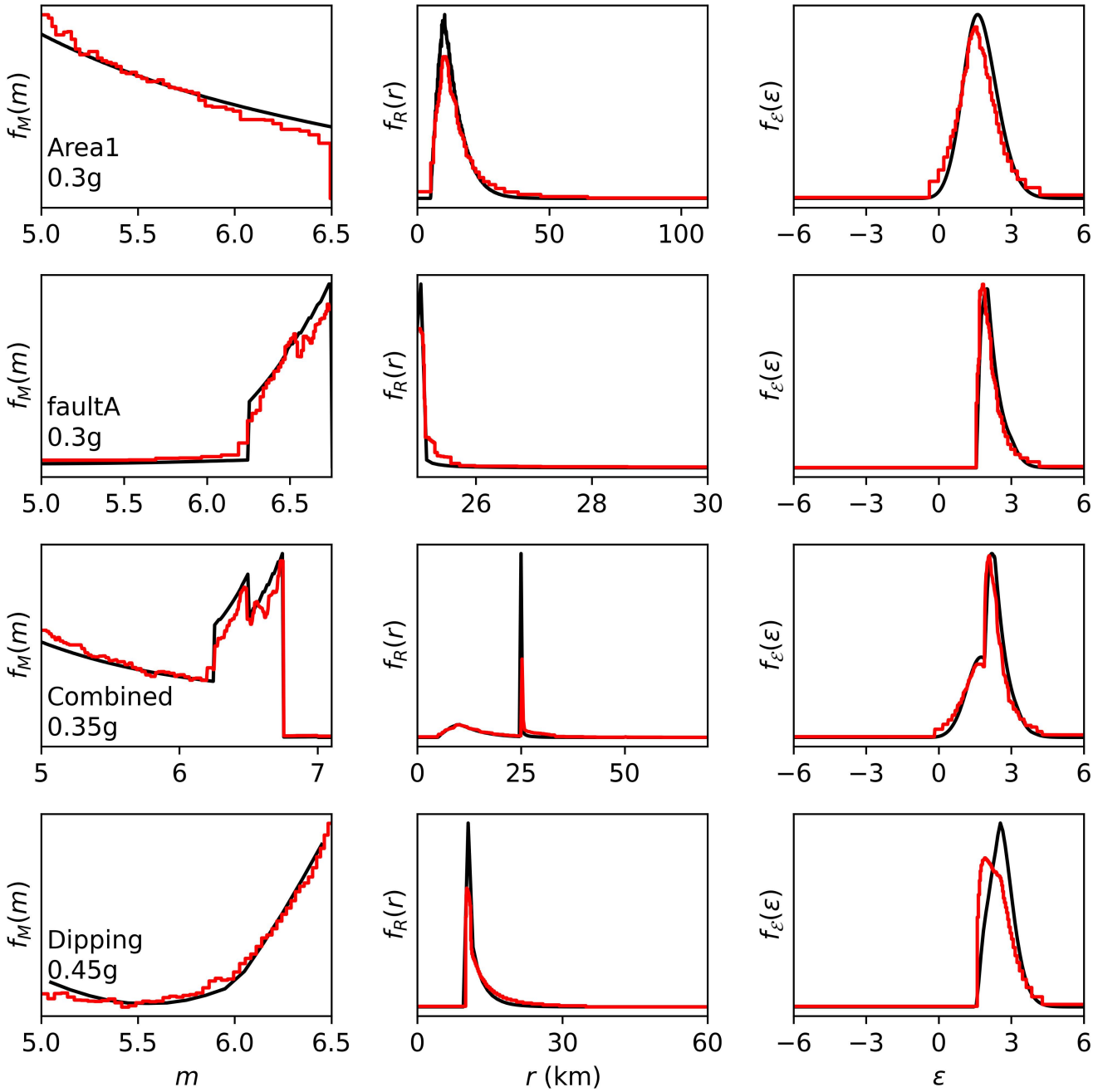

Figure 6. Example 1-4 (Area (Area1), Vertical fault (FaultA), Combined, and Dipping fault (FaultC) sources example): The convergence of m, r, and ε iterated IS densities (red) derived in AIS algorithm to marginal distributions of hazard disaggregation (black).

$$f_S(s) = \begin{cases} 0 & s < 0 \\ P(S = i) & \text{if } i - 1 \leq s < i \ \ (i = 1, 2, ..., n_s), \\ 0 & s \geq n_s \end{cases}$$

$f_S(s)$ is a piece-wise constant function where the heights are proportional to the corresponding sources' earthquake occurrence rates. We introduce $f_S(s)$ into the PSHA integration and obtain

$$\Lambda(X > a) = \left(\sum_i^{n_s} \nu_i\right) \int_s \int_\varepsilon \int_r \int_m I(x > a|s, m, r, \varepsilon) f_{M,R,\mathcal{E}}(m, r, \varepsilon|s) f_S(s) dm\, dr\, d\varepsilon\, ds. \tag{25}$$

Solving Eq. (25) posits computational challenges than the single source problems because $f_S(s)$ have the large jumps at $i = 1, 2, \ldots, n_s - 1$, and additional dependencies of m, r, and s are introduced. This could further diminish the VEGAS algorithm's effectiveness. Thus, we test two AIS PSHA approaches for this case: 1) full AIS approach utilizing the Eq. (25) and 2) partial AIS approach, which is the simple summation of single-source AIS PSHA curves.

We compared the computational performance of MC, IS, and full and partial AIS (Figure 4; see Figure S10 for the results on the other ground motion levels). Like the previous examples, conventional MC is faster for low ground motions, but not high ones. To achieve COV of 1 % at a ground motion of 0.35 g, corresponding to $\sim 1.2 \times 10^{-4}$ annual probability, conventional MC, IS, and full and partial AIS take 8.33, 891, 10.4, and 0.43 seconds, respectively, i.e., partial AIS is the most efficient algorithm, $\sim$ 19, 2,087, and 24 times faster than conventional MC, uniform IS, and full AIS, respectively. At more extreme 0.8 g case, conventional MC, IS, and full and partial AIS take 295, 49, 3.04, and 0.39 seconds, respectively; partial AIS is $\sim$ 756, 127, and 8 times faster than conventional MC, uniform IS, and full AIS, respectively.

Figures S11 and S12 present the accuracy of both AIS approaches with different sample sizes. The contrast between Figures S11 (c) S12 (c) shows that partial AIS has smaller error than full AIS even with fewer samples (N_s 150,000 < 500,000). For partial AIS, it estimates the true hazard curve at 2.5 % and 1.0 % COV when N_s is $\sim$ 150,000 and 300,000, respectively (Figure S12).

The hazard disaggregation results, compared with the proposed IS density obtained from partial AIS PSHA, are also shown in Figure 6 (see Figure S13 for the results on the other ground motion levels). Similar to the previous examples, the proposed IS density effectively captures the complex features of the disaggregation.

Example 4: Dipping fault source

We also tested our approach on a dipping fault passing beneath the site and GMM of Abrahamson et al. (2014). AIS also performs efficiently for this example (Figure 4; see Figure S14 for the results on the other ground motion levels). To achieve a 1% COV at 0.45 g-corresponding to an annual probability of 10^{-4}-AIS is 1.9, 2.4, and 683 times faster than uniform-IS, MC, and the Riemann Sum, respectively. At 1.0 g, AIS reaches higher efficiency and runs 4, 50, and 633 times faster than uniform-IS, MC, and the Riemann Sum, respectively. A comparison between the proposed IS density and the hazard disaggregation is also illustrated in Figure 6. Results for the other ground motion levels are available in Figure S15. Both generally exhibit similar trends, however, some differences observed in this example suggest that obtaining the proposed IS density exactly the same as the optimal density is a challenging task when dealing with highly correlated (m, r) distribution. Rather, we observe

a trade-off between the accuracy of m and ε densities. As the magnitude (m) IS density gives a higher contribution at large magnitudes than the actual disaggregation, the ε IS density slightly shifted to lower values than the actual disaggregation. Although differences are apparent in this example, it is important to note that we employed an extremely fine discretization for the comparison. This discrepancy may not be significant when using the coarser grids typically adopted for engineering applications (U. S. Nuclear Regulatory Commission, 2007; Petersen et al., 2024).

Example 5: Smart Riemann Sum versus Smart AIS PSHA

In the previous sections, we compared the efficiency and accuracy of various numerical solutions with AIS PSHA. Here, we extend this comparison by examining the performance of AIS PSHA against an advanced variant of Reimann sum, sometimes adopted by PSHA software packages to tackle computational burden (Ordaz et al., 2013). For this comparison, we use an enhanced version of AIS PSHA that leverages the information from similar ground motions to reduce computational times that otherwise would linearly increase with the number of ground motions of interest (N_a).

Smart Riemann Sum The smart Riemann Sum essentially follows the same approach as Eq. (8) but incorporates three primary modifications.

First, the summation over the distance, $\sum_r$, is replaced by a summation over rupture locations (latitude, longitude, and depth), $\sum_\phi \sum_\psi \sum_z$, accounting for the variety of distance metrics used in modern GMMs, such as R_{rup}, R_{JB}, R_x, etc. Second, $I(\cdot)$ is replaced by $P(X > a|m, \phi, \psi, z)$, which represents the probability that simulated ground motion exceeds the pre-defined threshold, a. $P(\cdot)$ can be computed using a pre-computed table of normal distribution CDF or rational Chebyshev approximation algorithm (Cody, 1969), significantly reducing the computational burden compared to brute-force integration over ε. The third modification involves the use of varying bin sizes in the spatial domain, or a smart-grid. Finer bins are used closer to the site, while coarser bins are used at greater distances owing to the reduction in hazard sensitivity to changes in rupture location at farther distances. A common strategy for this is logarithmic uniform spacing (Appendix C). Incorporating these three modifications results in a revised version of the Riemann Sum PSHA, as shown below:

$$\lambda(X > a) = \nu \sum_{l=1}^{N_z} \sum_{k=1}^{N_\psi} \sum_{j=1}^{N_\phi} \sum_{i=1}^{N_m} P(X > a|m_i, \phi_j, \psi_k, z_l)\, f_{M,\Phi,\Psi,Z}(m_i, \phi_j, \psi_k, z_l) \Delta m \Delta\phi_j(r) \Delta\psi_k(r) \Delta z \tag{26}$$

Smart AIS PSHA The AIS PSHA approach presented earlier uses a uniform distribution as the initial IS density. With the smart AIS PSHA, however, we compute the hazard sequentially from the lowest to the highest ground motion levels. Thus, we can utilize the iterated IS density obtained at a previous ground motion intensity as the initial IS density for the next (slightly higher) ground motion, e.g., approximated q^* for the hazard rate at 0.2g as initial IS density for 0.3g. While this approach cannot be applied at the lowest ground motion intensity, it is worth noting that determining the optimal density at extremely low ground motion levels is a trivial problem as $I(\cdot) \equiv 1$ (Eq. (19)). This smart approach reduces the number

of iterations required to approximate the optimal density, further enhancing computational efficiency while maintaining its robustness.

Numerical Example In this section, we compare the efficiency and accuracy of the smart Riemann Sum, (naive) AIS, and the smart AIS using PSHA test problem 1.10 from Hale et al. (2018) (Fig. 2 (e)). For this example, the low probability hazard is reported to be highly sensitive to the starting point of the Riemann-sum grids since the site only has the sources on one side.

Like naive Riemann Sum, the efficiency of the smart Riemann Sum is dependent on the spatial grid spacing, with a trade-off between the computational efficiency and estimation accuracy. To estimate COV of the smart Riemann Sum at a given grid structure, we assess the variability of the hazard estimates with respect to the randomized locations within each grid cell, as the error metric for the smart Riemann Sum at a given grid structure.

For spatial grid spacing of smart Riemann Sum, we conducted multiple sensitivity tests and determined that a magnitude bin size of 0.1 is sufficiently small. With this magnitude bin size, we evaluated the hazard computation time and COV for varying spatial log-uniform bin sizes (δ in Appendix C) of 0.01, 0.02, 0.03, 0.04, 0.05, 0.07, 0.1, and 0.2.

Our findings indicate that AIS outperforms the smart Riemann Sum, consistent with previous numerical examples, particularly in estimating low-probability hazards (Figure 7; see Figure S16 for the results on the other ground motion levels). For example, at 1.0 g ($\sim 10^{-6}$/year), achieving a COV of 1% requires computation times that are 43 and 130 times faster with naive AIS and smart AIS, respectively, compared to the smart Riemann Sum. At lower ground motions (e.g., 0.001 g), the Riemann Sum proves to be more efficient than AIS (Figure S16). It is important to note that the Riemann Sum uses the same grid spacing for all ground motion intensities to eliminate the need for repeated ground motion simulations. Therefore, to ensure hazard accuracy across all ground motion levels, it is fair to compare the Riemann Sum based on its worst-case performance, i.e., at 1.0 g.

Here, we note that identifying the "optimal" grid settings for Riemann Sum necessitates many sensitivity analyses based on grid size, introducing an additional computational burden, and our comparison does not account for the time required for these analyses. On the other hand, AIS allows for error estimation using Eq. (18) to compute the error of AIS hazard without running the code repeatedly, which is also one of the benefits of using AIS.

We also observed that the accuracy of the Riemann Sum saturates at different levels for various ground motion intensities (Figure 7). This residual error appears to be from coarse gridding at greater distances inherent in log-uniform spacing. While log-uniform spacing significantly enhances the efficiency of the Riemann Sum, it introduces irreducible errors that cannot be mitigated. In contrast, with AIS and smart AIS, increasing the number of samples, proportional to the computation time, leads to an exponential reduction in error.

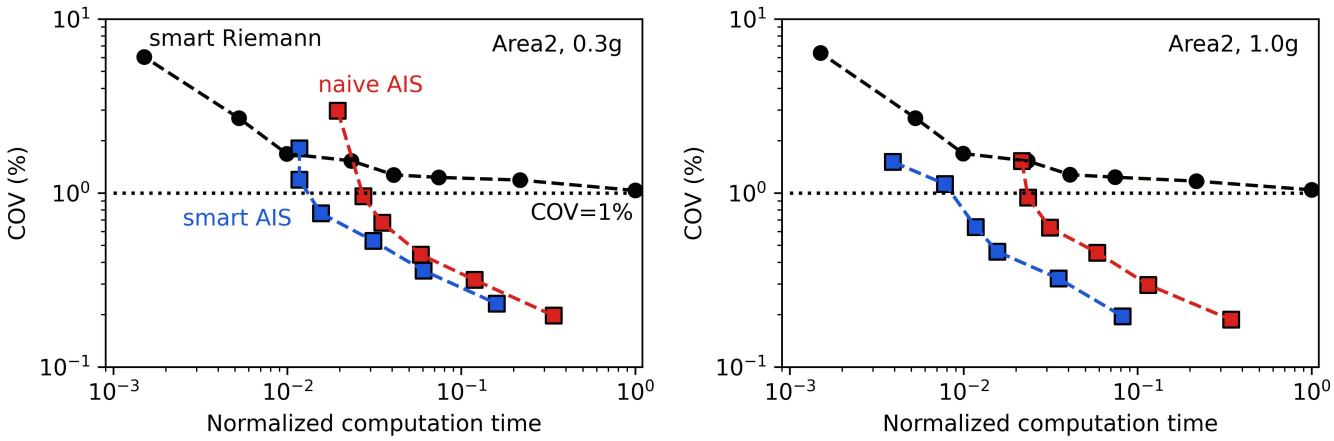

Figure 7. COV of smart Riemann Sum (black), AIS (red), and smart AIS (blue) hazard estimates as functions of computation time at ground motions of 0.3 g and 1.0 g, corresponding to $\sim 10^{-4}$/yr and 10^{-6}/yr, respectively.

AIS PSHA: POTENTIAL IMPACT ON PRACTICAL APPLICATION

We tested the AIS PSHA using various numerical examples; however, there are many more complex cases encountered in practice. In this section, we discuss how PSHA model complexity might affect the computational efficiency of AIS PSHA from two perspectives: (1) the propagation of epistemic uncertainty and (2) the use of more sophisticated seismic source and ground motion models.

In practice, researchers typically set multiple models and parameters to propagate the epistemic uncertainty of seismic hazards by organizing these into a logic-tree structure. The total computation time required to obtain the mean hazard and its percentiles is the product of the time needed to compute an individual hazard curve and the number of logic-tree end branches. Thus, any reduction in computation time for a single PSHA curve using our proposed approach also proportionally reduces the total computation time for calculating the mean and percentiles. This paper also demonstrated how to incorporate discrete probability distribution into the AIS framework in the combined sources example. This approach can similarly be applied to logic trees to model groups of branches simultaneously. However, readers should note that the full AIS strategy, which incorporates all elements into the VEGAS AIS framework, may sometimes be less efficient than calculating individual hazard curves separately and summing them, the partial AIS strategy, due to the increased dependencies among variables. While we could modify the algorithm to account for variable dependencies at an additional computational cost, we consider this an exciting area for future research beyond the scope of this study.

Furthermore, modern seismic source models are becoming more complex as knowledge of seismogenic faults accumulates (e.g., UCERF3; Field et al. (2014)). These complex models may introduce additional dependencies among variables, which could reduce the efficiency of VEGAS AIS, as demonstrated in the floating rupture fault source examples (numerical examples 2 and 4). However, the dependency of the distance distribution given magnitude decreases rapidly as the distance to the

source grows, implying that m and r can be treated as independent. In these cases, VEGAS AIS remains highly efficient. In fact, our examples represent worst-case scenarios in terms of AIS efficiency since the site is located close to the fault.

Similarly, modern ground motion models (GMMs) can increase the computational burden of PSHA. Recent empirical GMMs incorporate numerous additional terms to capture physical mechanisms not considered before (e.g., directivity effects, hanging-wall effects, depth to bedrock), increasing the number of coefficients by a factor of ∼10 (Bommer et al., 2010). In some recent PSHA projects, researchers have adopted physics-based ground motion simulations (Milner et al., 2021), further raising computational demands. AIS can mitigate the increased computational burden associated with complex ground motion models, as AIS requires fewer ground motion samples than traditional numerical methods. Moreover, the computation time for updating the IS density—a unique feature of AIS—remains constant regardless of model complexity (Figure S17).

CONCLUSION

We proposed a novel computational framework for PSHA based on an implementation of the VEGAS algorithm. Through comprehensive testbeds, we investigated the computational performance of this new approach, covering widely adopted source types in PSHA practice, including area, vertical and dipping fault, and combined sources.

We compared the proposed method to three existing computational frameworks: a) Riemann Sum, which has exponentially increasing computational costs for finer grid sizes; b) conventional MC, which requires a substantially long catalog with synthetic earthquakes, particularly for large seismic intensities; and c) importance sampling (IS) with simple (uniform) IS distributions.

Our findings indicate that AIS PSHA outperforms all other computational frameworks. AIS PSHA can dramatically reduce computational times by factors up to $\sim 3.7 \times 10^4$ compared to traditional Riemann Sum. AIS PSHA was also 7.1×10^3 faster than the conventional MC while maintaining a 1% COV. Additionally, AIS PSHA was up to 70 times faster than IS PSHA, demonstrating that the VEGAS algorithm can approximate optimal IS distributions quickly and well.

We showed that AIS PSHA requires a similar computation time for any ground motion, making its application to larger ground motions with low probability substantially more efficient than conventional MC. In PSHA practice, the computational demands are dominated by large ground motions that need substantially more samples than lower ground motions. In contrast, AIS PSHA only requires a similarly low number of samples for all ground motion levels because it finds optimized IS distributions for each.

We also showed that AIS PSHA finds approximated disaggregation curves at no extra computational cost based on theoretical insights showing that optimal IS densities are equivalent to disaggregation distributions. We showed empirically that the hazard disaggregation and iterated IS densities from AIS PSHA are fairly similar by comparing the statistical properties of the two distributions, e.g., K-S D statistics < 0.113 and mean values differences of <4.3 %.

Our study indicated that our AIS PSHA implementation works extremely well for point sources, where the magnitude and distance are independent random variables. We also applied the algorithm to problems employing the finite-rupture model, and it still outperformed the pre-existing algorithms up to by factors of >2,000. It appears to be less effective than the point source example because it introduces a dependency between the magnitude and distance. Our implementation of the VEGAS algorithm uses independent random variables for the IS distribution, thus making it less effective for the finite-rupture case. However, future implementations can also consider other versions of AIS algorithms where the variables are correlated; though computational demands for the AIS iteration would increase.

In the case of combined seismic sources, we proposed two strategies: 1) incorporating the source random variable into the AIS PSHA framework and 2) simple summation of AIS PSHA curves for individual sources. Both strategies outperformed the traditional methods up to by a factor of ~ 580. However, the second strategy was more efficient than the first one by a factor of 6. The first strategy added dependencies to the seismic hazard distribution, making the VEGAS less effective.

Additionally, we demonstrated that the algorithm can be even more efficient through a "smart" AIS, which uses the initial guess as the proposed IS density from adjacent ground motion intensity. Our findings indicate that this "smart" AIS demonstrates up to a 130-fold improvement in efficiency compared to the Riemann Sum with optimized spatial grid spacing.

In sum, AIS can be applied to any PSHA computation, leading us to expect widespread application of the method. Specifically, we consider our proposed AIS PSHA to be significantly beneficial for large-scale projects that involve numerous logic tree branches and have extreme computational demands.

DATA AND RESOURCES

The source code for computing PSHA using the framework explained in this paper is available at https://github.com/sehoung/ais_psha. Figures were created using Matplotlib (Hunter, 2007) and Microsoft PowerPoint (http://office.microsoft.com; last accessed June 2024). Supplemental Material for this article includes one Text, one Algorithm, one Table, and 17 Figures: Text S1 presents an explanation of the VEGAS AIS algorithm, Algorithm S1 shows the pseudocode of VEGAS AIS PSHA, Table S1 shows model parameters of the numerical examples, Figure S1 shows the examples of K-S D statistics, Figures S2, S6, S10, S14, and S16 show COV as a function of computation time of various numerical solutions, Figures S3, S7, S11, and S12 show the box plot of AIS PSHA estimates, Figures S4, S8, S13, S15 show the convergence of iterated IS densities to the hazard disaggregation, Figures S5 and S9 present the K-S D statistic and mean difference between hazard disaggregation and the iterated IS density, and Figure S17 presents the contribution of each part of VEGAS AIS to the total computation time.

DECLARATION OF COMPETING INTERESTS

The authors have filed a patent application related to the method discussed in this paper. This application is relevant to the research presented and could represent a potential financial interest.

ACKNOWLEDGMENTS

The authors acknowledge the financial support provided by the Tandon School of Engineering at New York University and the Department of Civil and Environmental Engineering at the University of California, Berkeley. We extend our gratitude to Ziqi Wang of the Department of Civil and Environmental Engineering at UC Berkeley for his insights on the mathematical derivations presented in this study. We also thank the associate editor, Dr. Céline Beauval, and the anonymous reviewers for their constructive comments and suggestions on this article.

REFERENCES

Abrahamson, N. A., W. J. Silva, and R. Kamai (2014). Summary of the ask14 ground motion relation for active crustal regions. *Earthquake Spectra* **30**(3), 1025–1055.

Alwall, J., R. Frederix, S. Frixione, V. Hirschi, F. Maltoni, O. Mattelaer, H.-S. Shao, T. Stelzer, P. Torrielli, and M. Zaro (2014). The automated computation of tree-level and next-to-leading order differential cross sections, and their matching to parton shower simulations. *Journal of High Energy Physics* **2014**(7), 1–157.

Arora, P. and L. Ceferino (2023). Probabilistic and machine learning methods for uncertainty quantification in power outage prediction due to extreme events. *Natural Hazards and Earth System Sciences* **23**(5), 1665–1683.

ASCE (2022). Minimum Design Loads for Buildings and Other Structures. ASCE/SEI Standard 7-22. American Society of Civil Engineering, Reston, Virginia.

Assatourians, K. and G. M. Atkinson (2013). EqHaz: An open-source probabilistic seismic-hazard code based on the Monte Carlo simulation approach. *Seismological Research Letters* **84**(3), 516–524.

Assatourians, K. and G. M. Atkinson (2019). Implementation of a smoothed-seismicity algorithm in Monte Carlo PSHA software EQHAZ and implications for localization of hazard in the Western Canada sedimentary basin. *Seismological Research Letters* **90**(3), 1407–1419.

Au, S.-K. and J. L. Beck (2001). Estimation of small failure probabilities in high dimensions by subset simulation. *Probabilistic engineering mechanics* **16**(4), 263–277.

Baker, J., B. Bradley, and P. Stafford (2021). *Seismic Hazard and Risk Analysis.* Cambridge University Press.

Bazzurro, P. and C. A. Cornell (1999). Disaggregation of seismic hazard. *Bulletin of the Seismological Society of America* **89**(2), 501–520.

Bommer, J. J. and N. A. Abrahamson (2006). Why do modern probabilistic seismic-hazard analyses often lead to increased hazard estimates? *Bulletin of the Seismological Society of America* **96**(6), 1967–1977.

Bommer, J. J., J. Douglas, F. Scherbaum, F. Cotton, H. Bungum, and D. Fah (2010). On the selection of ground-motion prediction equations for seismic hazard analysis. *Seismological Research Letters* **81**(5), 783–793.

Bozorgnia, Y., N. A. Abrahamson, L. A. Atik, T. D. Ancheta, G. M. Atkinson, J. W. Baker, A. Baltay, D. M. Boore, K. W. Campbell, B. S.-J. Chiou, et al. (2014). Nga-west2 research project. *Earthquake Spectra* **30**(3), 973–987.

Bugallo, M. F., V. Elvira, L. Martino, D. Luengo, J. Miguez, and P. M. Djuric (2017). Adaptive Importance Sampling: The past, the present, and the future. *IEEE Signal Processing Magazine* **34**(4), 60–79.

Campolieti, G. and R. Makarov (2007). Pricing path-dependent options on state dependent volatility models with a bessel bridge. *International Journal of Theoretical and Applied Finance* **10**(1), 51–88.

Ceferino, L., J. Mitrani-Reiser, A. Kiremidjian, G. Deierlein, and C. Bambarén (2020). Effective plans for hospital system response to earthquake emergencies. *Nature Communications* **11**(1), 4325.

Christou, V., P. Bocchini, M. J. Miranda, and A. Karamlou (2018). Effective sampling of spatially correlated intensity maps using hazard quantization: Application to seismic events. *ASCE-ASME Journal of Risk and Uncertainty in Engineering Systems, Part A: Civil Engineering* **4**(1), 04017035.

Cody, W. J. (1969). Rational chebyshev approximations for the error function. *Mathematics of computation* **23**(107), 631–637.

Coppersmith, K., J. Bommer, K. Hanson, J. Unruh, R. Coppersmith, L. Wolf, R. Youngs, A. Rodriguez-Marek, L. Al Atik, G. Toro, et al. (2014). Hanford Sitewide Probabilistic Seismic Hazard Analysis. PNNL-23361 Pacific Northwest National Laboratory, Richland Washington.

Cornell, C. A. (1968). Engineering seismic risk analysis. *Bulletin of the Seismological Society of America* **58**(5), 1583–1606.

Crowley, H. and J. J. Bommer (2006). Modelling seismic hazard in earthquake loss models with spatially distributed exposure. *Bulletin of Earthquake Engineering* **4**, 249–273.

Dick, J., F. Y. Kuo, and I. H. Sloan (2013). High-dimensional integration: The quasi-Monte Carlo way. *Acta Numerica* **22**, 133–288.

Field, E. H., R. J. Arrowsmith, G. P. Biasi, P. Bird, T. E. Dawson, K. R. Felzer, D. D. Jackson, K. M. Johnson, T. H. Jordan, C. Madden, et al. (2014). Uniform california earthquake rupture forecast, version 3 (ucerf3)—the time-independent model. *Bulletin of the Seismological Society of America* **104**(3), 1122–1180.

Field, E. H., T. H. Jordan, and C. A. Cornell (2003). OpenSHA: A developing community-modeling environment for seismic hazard analysis. *Seismological Research Letters* **74**(4), 406–419.

Friedman, J. H. and M. H. Wright (1981). A nested partitioning procedure for numerical multiple integration. *ACM Transactions on Mathematical Software (TOMS)* **7**(1), 76–92.

Garberoglio, G. and A. H. Harvey (2011). Path-integral calculation of the third virial coefficient of quantum gases at low temperatures. *The Journal of chemical physics* **134**(13), 134106.

Goulet, C. A., Y. Bozorgnia, N. Kuehn, L. Al Atik, R. R. Youngs, R. W. Graves, and G. M. Atkinson (2021). Nga-east ground-motion characterization model part i: Summary of products and model development. *Earthquake Spectra* **37**(1), 1231–1282.

Hale, C., N. Abrahamson, and Y. Bozorgnia (2018). Probabilistic Seismic Hazard Analysis Code Verification, PEER report 2018/03, Pacific Earthquake Engineering Research Center, Berkeley, CA.

Hammersley, J. M. and K. W. Morton (1954). Poor Man's Monte Carlo. *Journal of the Royal Statistical Society: Series B (Methodological)* **16**(1), 23–38.

Han, Y. and R. A. Davidson (2012). Probabilistic seismic hazard analysis for spatially distributed infrastructure. *Earthquake Engineering & Structural Dynamics* **41**(15), 2141–2158.

Hunter, J. D. (2007). Matplotlib: A 2d graphics environment. *Computing in science & engineering* **9**(03), 90–95.

Jayaram, N. and J. W. Baker (2010). Efficient sampling and data reduction techniques for probabilistic seismic lifeline risk assessment. *Earthquake Engineering & Structural Dynamics* **39**(10), 1109–1131.

Kappen, H. J. and H. C. Ruiz (2016). Adaptive importance sampling for control and inference. *Journal of Statistical Physics* **162**, 1244–1266.

Kavvada, I., S. Moura, A. Horvath, and N. Abrahamson (2022). Probabilistic seismic hazard analysis for spatially distributed infrastructure considering the correlation of spectral acceleration across spectral periods. *Earthquake Spectra* **38**(2), 1148–1175.

Kennedy, R. P., C. A. Cornell, R. D. Campbell, S. Kaplan, and H. F. Perla (1980). Probabilistic seismic safety study of an existing nuclear power plant. *Nuclear Engineering and Design* **59**(2), 315–338.

Kersevan, B. P. and E. Richter-Was (2013). The monte carlo event generator acermc versions 2.0 to 3.8 with interfaces to pythia 6.4, herwig 6.5 and ariadne 4.1. *Computer Physics Communications* **184**(3), 919–985.

Kiremidjian, A. S., H. C. Shah, and P. L. Sutch (1982). Seismic hazard and uncertainty analysis of honduras. *International Journal of Soil Dynamics and Earthquake Engineering* **1**(2), 83–94.

Kiremidjian, A. S., E. Stergiou, and R. Lee (2007). Issues in seismic risk assessment of transportation networks. *Geotechnical, Geological and Earthquake Engineering* **6**, 461–480.

Kolmogorov, A. (1933). Sulla determinazione empirica di una legge didistribuzione. *Giorn Dell'inst Ital Degli Att* **4**, 89–91.

Kroese, D. P., T. Brereton, T. Taimre, and Z. I. Botev (2014). Why the Monte Carlo method is so important today. *Wiley Interdisciplinary Reviews: Computational Statistics* **6**(6), 386–392.

Lepage, G. (1978). A new algorithm for adaptive multidimensional integration. *Journal of Computational Physics* **27**(2), 192–203.

Lepage, G. P. (2021). Adaptive multidimensional integration: vegas enhanced. *Journal of Computational Physics* **439**, 110386.

Manzour, H., R. A. Davidson, N. Horspool, and L. K. Nozick (2016). Seismic hazard and loss analysis for spatially distributed infrastructure in Christchurch, New Zealand. *Earthquake Spectra* **32**(2), 697–712.

McGuire, R. K. (1976). FORTRAN computer program for seismic risk analysis. USGS Open-File Report 76-67.

McGuire, R. K. (1995). Probabilistic seismic hazard analysis and design earthquakes: closing the loop. *Bulletin of the Seismological Society of America* **85**(5), 1275–1284.

McGuire, R. K. (2008). Probabilistic seismic hazard analysis: Early history. *Earthquake Engineering and Structural Dynamics* **37**(3), 329–338.

Milner, K. R., B. E. Shaw, C. A. Goulet, K. B. Richards-Dinger, S. Callaghan, T. H. Jordan, J. H. Dieterich, and E. H. Field (2021). Toward physics-based nonergodic psha: A prototype fully deterministic seismic hazard model for southern california. *Bulletin of the Seismological Society of America* **111**(2), 898–915.

Musson, R. M. W. (2000). The use of Monte Carlo simulations for seismic hazard assessment in the UK. *Annals of Geophysics* **43**(1), 1–9.

Nieto, M. R. and E. Ruiz (2016). Frontiers in var forecasting and backtesting. *International Journal of Forecasting* **32**(2), 475–501.

Novak, E. and K. Ritter (1997). The curse of dimension and a universal method for numerical integration. In *Multivariate approximation and splines*, pp. 177–187. Springer.

Ordaz, M., F. Martinelli, V. D'Amico, and C. Meletti (2013). CRISIS2008: A flexible tool to perform probabilistic seismic hazard assessment. *Seismological Research Letters* **84**(3), 495–504.

Ordaz, M., F. Martinelli, V. D'Amico, and C. Meletti (2013). Crisis2008: A flexible tool to perform probabilistic seismic hazard assessment. *Seismological Research Letters* **84**(3), 495–504.

Pagani, M., D. Monelli, G. Weatherill, L. Danciu, H. Crowley, V. Silva, P. Henshaw, L. Butler, M. Nastasi, L. Panzeri, M. Simionato, and D. Vigano (2014). Openquake engine: An open hazard (and risk) software for the global earthquake model. *Seismological Research Letters* **85**(3), 692–702.

Papadopoulos, A. N. and P. Bazzurro (2021). Exploring probabilistic seismic risk assessment accounting for seismicity clustering and damage accumulation: Part II. Risk analysis. *Earthquake Spectra* **37**(1), 386–408.

Petersen, M. D., A. M. Shumway, P. M. Powers, E. H. Field, M. P. Moschetti, K. S. Jaiswal, K. R. Milner, S. Rezaeian, A. D. Frankel, A. L. Llenos, et al. (2024). The 2023 us 50-state national seismic hazard model: Overview and implications. *Earthquake Spectra* **40**(1), 5–88.

Philippe, A. and C. P. Robert (2001). Riemann sums for MCMC estimation and convergence monitoring. *Statistics and Computing* **11**(2), 103–115.

Press, W. H. and G. R. Farrar (1990). Recursive stratified sampling for multidimensional monte carlo integration. *Computers in Physics* **4**(2), 190–195.

Rahimi, H. and M. Mahsuli (2019). Structural reliability approach to analysis of probabilistic seismic hazard and its sensitivities. *Bulletin of Earthquake Engineering* **17**(3), 1331–1359.

Ray, J., Y. Marzouk, and H. Najm (2011). A bayesian approach for estimating bioterror attacks from patient data. *Statistics in Medicine* **30**(2), 101–126.

Robert, C. P., G. Casella, and G. Casella (1999). *Monte Carlo statistical methods*, Volume 2. Springer.

Rubinstein, R. Y. (1997). Optimization of computer simulation models with rare events. *European Journal of Operational Research* **99**(1), 89–112.

Rubinstein, R. Y. and D. P. Kroese (2004). *The cross-entropy method: a unified approach to combinatorial optimization, Monte-Carlo simulation, and machine learning*. Springer.

Sadigh, K., C. Y. Chang, J. A. Egan, F. Makdisi, and R. R. Youngs (1997). Attenuation relationships for shallow crustal earthquakes based on California strong motion data. *Seismological Research Letters* **68**(1), 180–189.

Sanders, J. L. (2014). Probabilistic model for constraining the galactic potential using tidal streams. *Monthly Notices of the Royal Astronomical Society* **443**(1), 423–431.

Silva, V., D. Amo-Oduro, A. Calderon, C. Costa, J. Dabbeek, V. Despotaki, L. Martins, M. Pagani, A. Rao, M. Simionato, D. Viganò, C. Yepes-Estrada, A. Acevedo, H. Crowley, N. Horspool, K. Jaiswal, M. Journeay, and M. Pittore (2020). Development of a global seismic risk model. *Earthquake Spectra* **36**, 372–394.

Thomas, P., I. Wong, and N. A. Abrahamson (2010). Verification of probabilistic seismic hazard analysis computer programs. PEER Report 2010/106, Pacific Earthquake Engineering Research Center, Berkeley.

Tokdar, S. T. and R. E. Kass (2010). Importance sampling: A review. *Wiley Interdisciplinary Reviews: Computational Statistics* **2**(1), 54–60.

U. S. Nuclear Regulatory Commission (2007). A Performance Based Approach to Define Site Specific Ground Motion. Regulatory Guide 1.208, USNRC.

LIST OF FIGURE CAPTIONS

- **Figure 1**. VEGAS iterations of IS density in our AIS PSHA framework. Example for PSHA at PGA = 0.5 g when the site is located 10 km away from a point seismic source ($m_{\min} = 5.0$, $m_{\max} = 8.0$, b-value = 1.0, $\nu = 1.0$/yr, Ground Motion Model (GMM) = Sadigh et al. (1997)). The total number of MC samples is 2,000, and the number of grids per axis is 10, constituting a total of 100 rectangles (cuboids in actual three-dimensional PSHA integration). The vertical and horizontal black solid lines are boundaries of the m and ε rectangles, and gray dots are the MC samples. Starting from the initial same-size m and ε rectangles, their sizes are adjusted depending on the contribution of each rectangle to the hazard. The final proposed structure of the rectangles gives a highly concentrated probability density at $m \sim 5$ and $\varepsilon \sim 2$. Note that the hazard estimates using initialized density, density after the first iteration, and the final proposed density are 0.0417, 0.0413, and 0.0378, while the true solution is 0.0385.
- **Figure 2**. Seismic source geometry for the numerical examples to test our AIS PSHA framework.
- **Figure 3**. Benchmark PSHA curves for area source 1, linear fault source, combined sources, dipping source, and areal source 2. The benchmark curves are obtained from either Hale et al. (2018) (for areal source 1, combined sources, and areal source 2) or calculation by the authors (linear fault source and dipping source).
- **Figure 4**. Example 1-4 (Area (Area1), Vertical fault (FaultA), Combined, and Dipping fault (FaultC) sources example): COV as a function of computation time using various PSHA numerical solutions at ground motion intensities that correspond to 10^{-4}/yr: 0.3g, 0.3g, 0.35g, and 0.45g for the area, fault, combined, dipping fault sources, respectively, and extreme ground motion intensities: 1.0g ($\sim 10^{-6}$/yr), 1.0g (2.62×10^{-8}/yr), 0.8g (3.11×10^{-6}/yr), and 1.0g (2.51×10^{-6}/yr) for area, vertical fault, combined, and dipping fault sources, respectively. COV of 1% is denoted as dotted horizontal lines. As the target ground motion increases, the performance of AIS makes a dramatic improvement in terms of both accuracy and computational cost.
- **Figure 5**. COV of MC estimates with the ground motion for conventional (red) MC ($N_{\mathrm{s,\,convMC}} = 10^7$) and AIS (black) with the similar computation time. The COV of error exponentially increases with the ground motion in conventional MC, while that of AIS remains constant.
- **Figure 6**. Example 1-4 (Area (Area1), Vertical fault (FaultA), Combined, and Dipping fault (FaultC) sources example): The convergence of m, r, and ε iterated IS densities (red) derived in AIS algorithm to marginal distributions of hazard disaggregation (black).
- **Figure 7**. COV of smart Riemann Sum (black), AIS (red), and smart AIS (blue) hazard estimates as functions of computation time at ground motions of 0.3 g and 1.0 g, corresponding to $\sim 10^{-4}$/yr and 10^{-6}/yr, respectively.

FULL MAILING ADDRESS FOR EACH AUTHOR

Soung Eil Houng

University of California, Berkeley

Department of Civil and Environmental Engineering

Davis Hall, Berkeley, 94720, CA

shoung@berkeley.edu

Luis Ceferino

University of California, Berkeley

Department of Civil and Environmental Engineering

Davis Hall, Berkeley, 94720, CA

ceferino@berkeley.edu

APPENDIX A: MEAN AND VARIANCE OF MONTE-CARLO PSHA ESTIMATE

The mean of MC hazard estimates, $\hat{\lambda}$, $E[\hat{\lambda}]$, can be derived as follows:

$$
\begin{aligned}
E[\hat{\lambda}] &= E\left[\frac{\nu}{N_s}\sum_{i=1}^{N_s} I(X_i > a|M_i, R_i, \mathcal{E}_i)\right] \\
&= \frac{\nu}{N_s}\sum_{i=1}^{N_s} E\left[I(X_i > a|M_i, R_i, \mathcal{E}_i)\right] \\
&= \frac{1}{N_s}\sum_{i=1}^{N_s} \nu \iiint I(X_i > a|m_i, r_i, \varepsilon_i) f_{M,R,\mathcal{E}}(m_i, r_i, \varepsilon_i) dm_i dr_i d\varepsilon_i \\
&= \frac{1}{N_s}\sum_{i=1}^{N_s} \lambda(X > a) \\
&= \lambda(X > a)
\end{aligned}
$$

The second moment of $\hat{\lambda}$, $E[\hat{\lambda}^2]$, can be expressed as:

$$
\begin{aligned}
E[\hat{\lambda}^2] &= E\left[\left(\frac{\nu}{N_s}\sum_{i}^{N_s} I(X_i > a)\right)^2\right] \\
&= \frac{\nu^2}{N_s^2} E\left[\left(\sum_{i}^{N_s} I_i\right)^2\right]
\end{aligned}
$$

, where $I(X_i > a)$ is denoted as I_i for simplicity in the following derivation. The above equation expands as follows:

$$
\begin{aligned}
E[\hat{\lambda}^2] &= \frac{\nu^2}{N_s^2} E\left[(I_1 + I_2 + \cdots + I_{N_s})^2\right] \\
&= \frac{\nu^2}{{N_s}^2} E[I_1^2 + I_2^2 + \cdots + I_{N_s}^2 \; + \; I_1 I_2 + I_1 I_3 + I_1 I_4 + \cdots + I_1 I_{N_s} \\
&\qquad + I_2 I_1 + I_2 I_3 + I_2 I_4 + \cdots + I_2 I_{N_s} \\
&\qquad + I_3 I_1 + I_3 I_2 + I_3 I_4 + \cdots + I_3 I_{N_s} \\
&\qquad \vdots \\
&\qquad + I_{N_s} I_1 + I_{N_s} I_2 + I_{N_s} I_3 + \cdots + I_{N_s} I_{N_s - 1}] \\
&= \frac{\nu^2}{{N_s}^2} E\left[\sum_{i}^{N_s} I_i^2 + \sum_{i \neq j}^{{N_s}^2 - N_s} I_i I_j\right]
\end{aligned}
$$

Here, I_i^2 is the same as I_i since I_i^2 also takes one if and only if X_i is greater than a. Also, the expectation operator can go inside the sum terms as it is a linear operator:

$$
E[\hat{\lambda}^2] = \frac{\nu}{{N_s}^2}\sum_{i}^{N_s} \nu E[I_i] + \frac{1}{{N_s}^2}\sum_{i \neq j}^{{N_s}^2 - N_s} \nu^2 E[I_i I_j]
$$

Here, $\nu E[I_i]$ is equal to λ. Also, $I_i\, I_j$ takes one if and only if both X_i and X_j exceed a. Given that the ground motion samples (X_i and X_j) are extracted independently, $\nu^2 E[I_i I_j]$ is identical to $\nu E[I_i]\nu E[I_j]$, which is λ^2:

$$
\begin{aligned}
E[\hat{\lambda}^2] &= \frac{\nu}{{N_s}^2}\sum_{i}^{N_s}\lambda + \frac{1}{{N_s}^2}\sum_{i\neq j}^{{N_s}^2-N_s}\lambda^2 \\
&= \frac{\nu\lambda-\lambda^2}{N_s}+\lambda^2
\end{aligned}
$$

Hence,

$$
\begin{aligned}
\mathrm{VAR}[\hat{\lambda}] &= E[\hat{\lambda}^2]-E[\hat{\lambda}]^2 \\
&= E\left[\hat{\lambda}^2\right]-\lambda^2 \\
&= \frac{\nu\lambda-\lambda^2}{N_s}
\end{aligned}
$$

APPENDIX B: MEAN AND VARIANCE OF IMPORTANCE SAMPLING PSHA ESTIMATE

The mean of IS hazard estimate, $\hat{\lambda}$, $E_q[\hat{\lambda}^2]$, can be derived as follows:

$$
\begin{aligned}
E_q[\hat{\lambda}] &= \frac{\nu}{N_s}\sum_{i=1}^{N_s} E_q\left[I(X_i>a|M_i,R_i,\mathcal{E}_i)\frac{f_{M,R,\mathcal{E}}(M_i,R_i,\mathcal{E}_i)}{q_{M,R,\mathcal{E}}(M_i,R_i,\mathcal{E}_i)}\right] \\
&= \frac{1}{N_s}\sum_{i=1}^{N_s}\nu\int I(X>a|m,r,\varepsilon)\frac{f_{M,R,\mathcal{E}}(m,r,\varepsilon)}{q_{M,R,\mathcal{E}}(m,r,\varepsilon)}q_{M,R,\mathcal{E}}(m,r,\varepsilon)dmdrd\varepsilon \\
&= \frac{1}{N_s}\sum_{i=1}^{N_s}\lambda \\
&= \lambda
\end{aligned}
\tag{27}
$$

Also, the second moment of $\hat{\lambda}$, $E_q[\hat{\lambda}^2]$, can be expressed as:

$$
\begin{aligned}
E_q[\hat{\lambda}^2] &= E_q\left[\left(\frac{\nu}{N_s}\sum_{i}^{N_s}\frac{I(X_i>a)f_{M,R,\mathcal{E}}(M_i,R_i,\mathcal{E}_i)}{q_{M,R,\mathcal{E}}(M_i,R_i,\mathcal{E}_i)}\right)^2\right] \\
&= \frac{\nu^2}{N_s^2}E_q\left[\left(\sum_{i}^{N_s}\frac{I_i f_i}{q_i}\right)^2\right]
\end{aligned}
$$

Note that $I(X_i>a)$, $f_{M,R,\mathcal{E}}(M_i,R_i,\mathcal{E}_i)$, and $q_{M,R,\mathcal{E}}(M_i,R_i,\mathcal{E}_i)$ are denoted as I_i, f_i, and q_i for simplicity in the following derivation. As derived in Appendix A, the above equation expands as follows:

$$
\begin{aligned}
E_q[\hat{\lambda}^2] &= \frac{\nu^2}{N_s^2} E_q \left[\sum_i^{N_s} \left(\frac{I_i f_i}{q_i} \right)^2 + \sum_{i \neq j}^{N_s^2 - N_s} \left(\frac{I_i f_i}{q_i} \right) \left(\frac{I_j f_j}{q_j} \right) \right] \\
&= \frac{\nu^2}{N_s^2} \sum_i^{N_s} E_q \left[\left(\frac{I_i f_i}{q_i} \right)^2 \right] + \frac{\nu^2}{N_s^2} \sum_{i \neq j}^{N_s^2 - N_s} E_q \left[\left(\frac{I_i f_i}{q_i} \right) \left(\frac{I_j f_j}{q_j} \right) \right] \\
&= \frac{\nu^2}{N_s} \frac{1}{N_s} \sum_i^{N_s} E_q \left[\left(\frac{I_i f_i}{q_i} \right)^2 \right] + \frac{1}{N_s^2} \sum_{i \neq j}^{N_s^2 - N_s} \nu E_q \left[\left(\frac{I_i f_i}{q_i} \right) \right] \nu E \left[\left(\frac{I_j f_j}{q_j} \right) \right] \\
&= \frac{\nu^2}{N_s} E_q \left[E_q \left[\left(\frac{I_i f_i}{q_i} \right)^2 \right] \right] + \frac{1}{N_s^2} (N_s^2 - N_s) \lambda^2 \\
&= \frac{\nu^2}{N_s} E_q \left[\left(\frac{I_i f_i}{q_i} \right)^2 \right] - \frac{1}{N_s} \lambda^2 + \lambda^2
\end{aligned}
$$

Hence,

$$
\begin{aligned}
\mathrm{VAR}[\hat{\lambda}] &= E_q[\hat{\lambda}^2] - E_q[\hat{\lambda}]^2 \\
&= \frac{1}{N_s} \left(\nu^2 E_q \left[\left(\frac{I_i f_i}{q_i} \right)^2 \right] - \lambda^2 \right)
\end{aligned}
$$

APPENDIX C: LOG-UNIFORM SPACING OF SPATIAL GRID

By adopting log-uniform spacing in the spatial domain, the ith grid size, i, can be calculated as:

$$
\Delta_i = 10^{\delta \cdot i} (10^{\delta} - 1)
$$

, where i is a positive integer increase with the distance from the site, is a constant representing the spacing interval in logarithmic scale (e.g., 0.1). Note that simply adopting Δ_i as $10^{\delta \cdot i}$ cannot capture the finer grid spacing at a distance less than one distance unit. The difference between kth and $(k+1)$th power of 10 allows us to generate a sufficiently fine grid at those distances. The grid spacing at source location X, r km away from the site location, $\Delta(X; r)$, is as follows:

$$
\Delta(X; r) = \Delta_i, \text{ such that } F_{i-1} \leq r < F_i
$$

, where F_i is the cumulative sum of the grids:

$$
F_i = \sum_{k=1}^{i} \Delta_k, \text{ i} = 1, 2, 3, 4, \ldots
$$

, where $F_0 = 0$.

Manuscript Received 00 Month 0000